

SOLID STATE IMAGE SENSING ARRAYS

G. SADASIV, PRINCIPAL INVESTIGATOR

FINAL TECHNICAL REPORT

DECEMBER 1, 1972

**CASE FILE
COPY**

NATIONAL AERONAUTICS AND SPACE ADMINISTRATION
WASHINGTON, D. C.

CONTRACT NO. - NGR-40-004-022

Department of Electrical Engineering
University of Rhode Island
Kingston, R. I. 02881

SOLID STATE IMAGE SENSING ARRAYS

G. SADASIV, PRINCIPAL INVESTIGATOR

FINAL TECHNICAL REPORT

DECEMBER 1, 1972

National Aeronautics and Space Administration
Washington, D.C.

CONTRACT NO.-NGR-40-004-022

Department of Electrical Engineering
University of Rhode Island
Kingston, R. I. 02881

TABLE OF CONTENTS

	Page
Abstract.	i
I. Introduction.	1
II. Photodiode Bipolar Transistor Array.	3
a. Operating Principles	3
b. Fabrication of Arrays	7
c. Tests on Individual Elements	21
III. Scanning Circuits for Image Sensing Arrays	27
IV. Optical - Absorption Edge of Silicon.	35
V. Heterojunctions	36
VI. Summary and Recommendations for Further Work.	40
VII. Faculty Participation	41
VIII. References.	42
IX. Figure Captions	43
APPENDIX I.	45

ABSTRACT

The fabrication of a photodiode transistor image sensor array in silicon, and tests on individual elements of the array are described. A design for a scanning system for an image sensor array is described.

The spectral response of p-n junctions was used as a technique for studying the optical-absorption edge in silicon

Heterojunction structures of Sb_2S_3 - Si were fabricated. A system for measuring C-V curves on MOS structures has been built.

I. INTRODUCTION

Solid state image sensors consist of arrays of radiation sensors connected by address strips to scan generators and coupling circuits. These permit the interrogation of individual elements to generate a video signal. During the past year research on solid state image sensors sponsored by NASA has been in progress in the Department of Electrical Engineering at the University of Rhode Island. The objective of the program has been to investigate novel designs for solid state image sensing arrays. This involves both the study of photoeffects in materials and devices to evaluate their suitability for sensor arrays and the design of novel structures compatible with feasible fabrication technology.

This report describes the progress achieved thus far. The main emphasis has been on arrays using silicon technology. Section II contains a discussion of the operating principles, fabrication procedures and tests on individual elements of a novel design for a photodiode-bipolar transistor array in silicon. The design of scanning circuits which are being built for use with this array is given in Section III. In studying the optical properties of silicon, it was found that the measurement of the spectral response of p-n junctions provided a very valuable technique for studying optical absorption at very low absorption levels. The results obtained are given in Section IV and a paper based on these results (to be published in Physical Review) is given as Appendix I.

Work on the photoeffects in heterojunctions made up of

Si - Sb_2S_3 - Au sandwiches is reported in Section V. The results on these samples were not reproducible and the cause was probably due to contamination of the silicon surface. An MOS-capacitance measurement system has been set up to study this problem.

II. PHOTODIODE BIPOLAR TRANSISTOR ARRAY

a. Principle of Operation

Each element in a solid state photosensor array must have a photosensing device, a switch to allow individual addressing and, preferably, an amplifier to increase the sensitivity¹. The most successful approach to date has been the utilization of a silicon phototransistor as the element. The collector diode of the transistor is used in the photon flux integration mode as the light sensor. The emitter diode is used as the switch. In addition to the gain due to storage, further amplification is achieved by the transistor action in the device. Arrays have also been fabricated using a photodiode as the sensor and an MOS transistor as the switch. In practice there are just arrays of MOS transistors, the source diode acting as the photosensitive junction.

Sensors in which the photodiode doubles as either source junction or collector junction are attractive in that they provide structures which readily lend themselves to integration into densely packed arrays. However, the dual function of the diode leads to limitations on the performance of the array. A design which would permit greater flexibility in individually optimizing the performance of sensor, switch and amplifier in the element is shown in Figure 1. In the figure the equivalent circuit for a few of the elements of the array is shown. The basic element consists of a photodiode and a bipolar transistor. The peripheral blocks represent scanning circuits which will be discussed later in Section III.

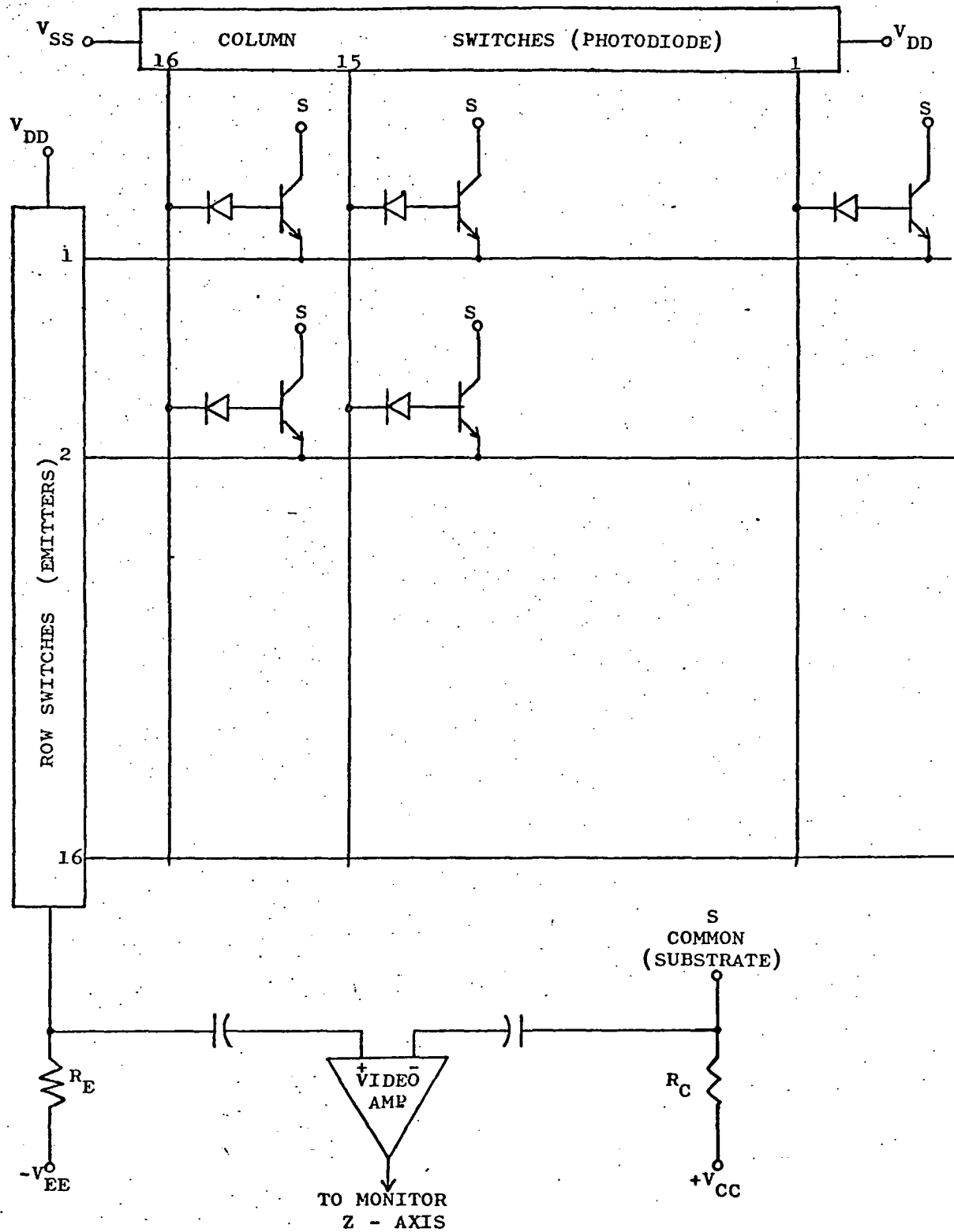


Fig. 1 Equivalent circuit for a photodiode-bipolar transistor image sensing array.

The operation of the element in the array is as follows. A combination of $+V_B$ volts on the column and 0 volts on the row selects one element. The photodiode is reverse biased and the depletion layer capacitance C is charged through the emitter of the transistor, as illustrated in Fig. 2. This constitutes the base current of the transistor and results in an amplified signal current in the collector circuit. At all times other than the scanning time, the combination of voltages are such that the photodiode remains isolated, and acts in the usual storage mode. In the interval between scans, the charge on C gets depleted through the reverse current of the photodiode and this charge is replaced in the next scanning period.

The video signal can be extracted from the array either from the common collector or from the emitter. In the latter case one would use a commutator to connect each row in turn to the video amplifier, as is indicated symbolically in Figure 1 by the row switching circuit. One advantage of having two points for getting the signal is as follows. When the array is being scanned row by row, the high speed switching transients from the pulses on the columns appear at the emitter and the collector load resistors via the base-emitter and base-collector capacitances respectively. The signal, on the other hand, appears in opposite phase at these two points. By feeding both outputs into a suitable differential amplifier, it is possible to improve the signal to switching transient ratio in the video signal.

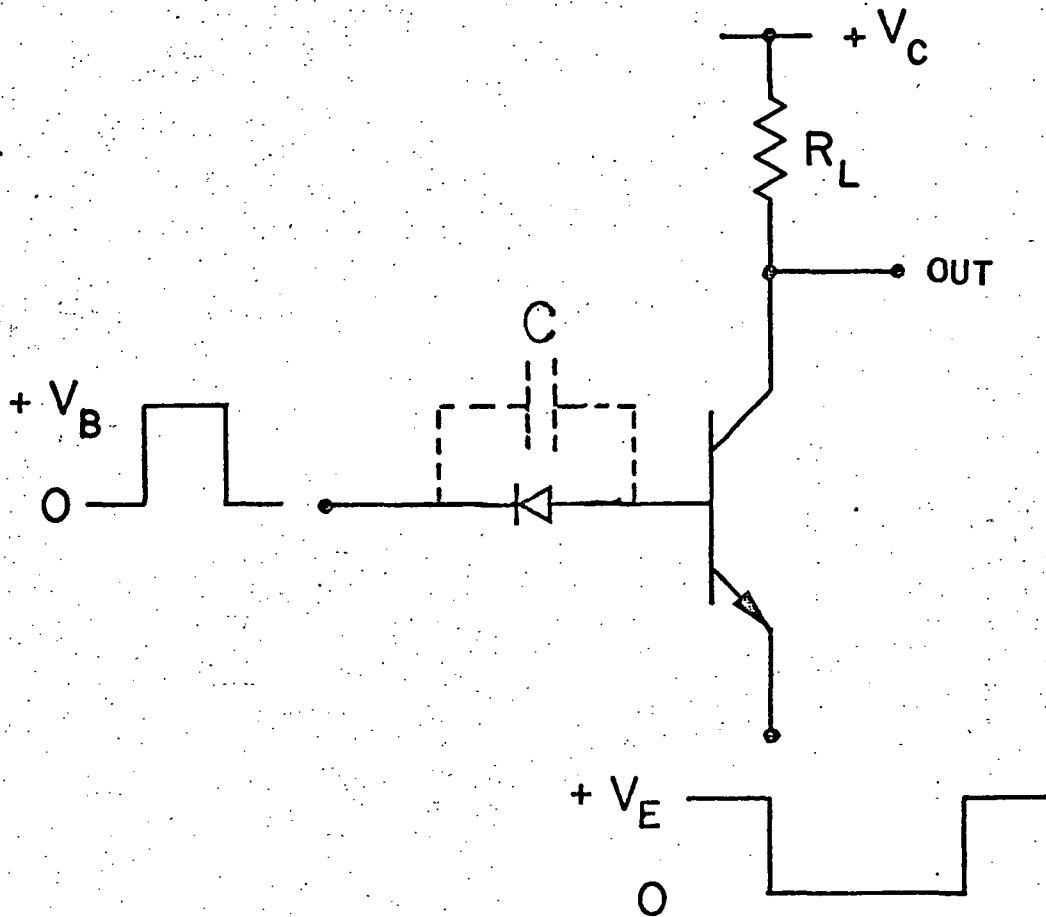


Fig. 2 Operation of a photodiode-bipolar transistor element.

b. Fabrication of photodiode-transistor image sensor

The fabrication of these arrays in silicon is compatible with conventional integrated circuit technology. A schematic integrated circuit layout for making these structures is shown in Figure 3. The basic processing steps are as follows. A deep p-type well is diffused into an n-type substrate in the region where the photodiode is to be formed. A shallow p-diffusion is made in the transistor region. The next step is an n-diffusion to form the emitter of the transistor and the cathode of the photodiode. Metallization with row and column busbars completes the fabrication.

The array permits great flexibility of design in that the diode and the transistor are formed separately and the fabrication of each can be optimized for the particular use of the array being considered. In order that the leakage currents and junction capacitances of the transistor be smaller than those of the photodiode, the area occupied by the transistor should be much smaller than that occupied by the photodiode. The metallization of the rows can be used to prevent the incident light from falling on the transistor region.

Several units have been fabricated. The fabrication included all diffusion steps; the final metallization steps have not yet been done. In making these arrays the geometry of the masks used has not been optimized. It was considered more advantageous in the present stage of the program to use commercially available inexpensive masks rather than make expensive custom-designed ones. Various standard masks, having squares and rectangles of different

sizes on 20 mil centers were used². The patterns thus covered the entire wafer, and coarse masks were used to isolate sections having 16 x 16 elements.

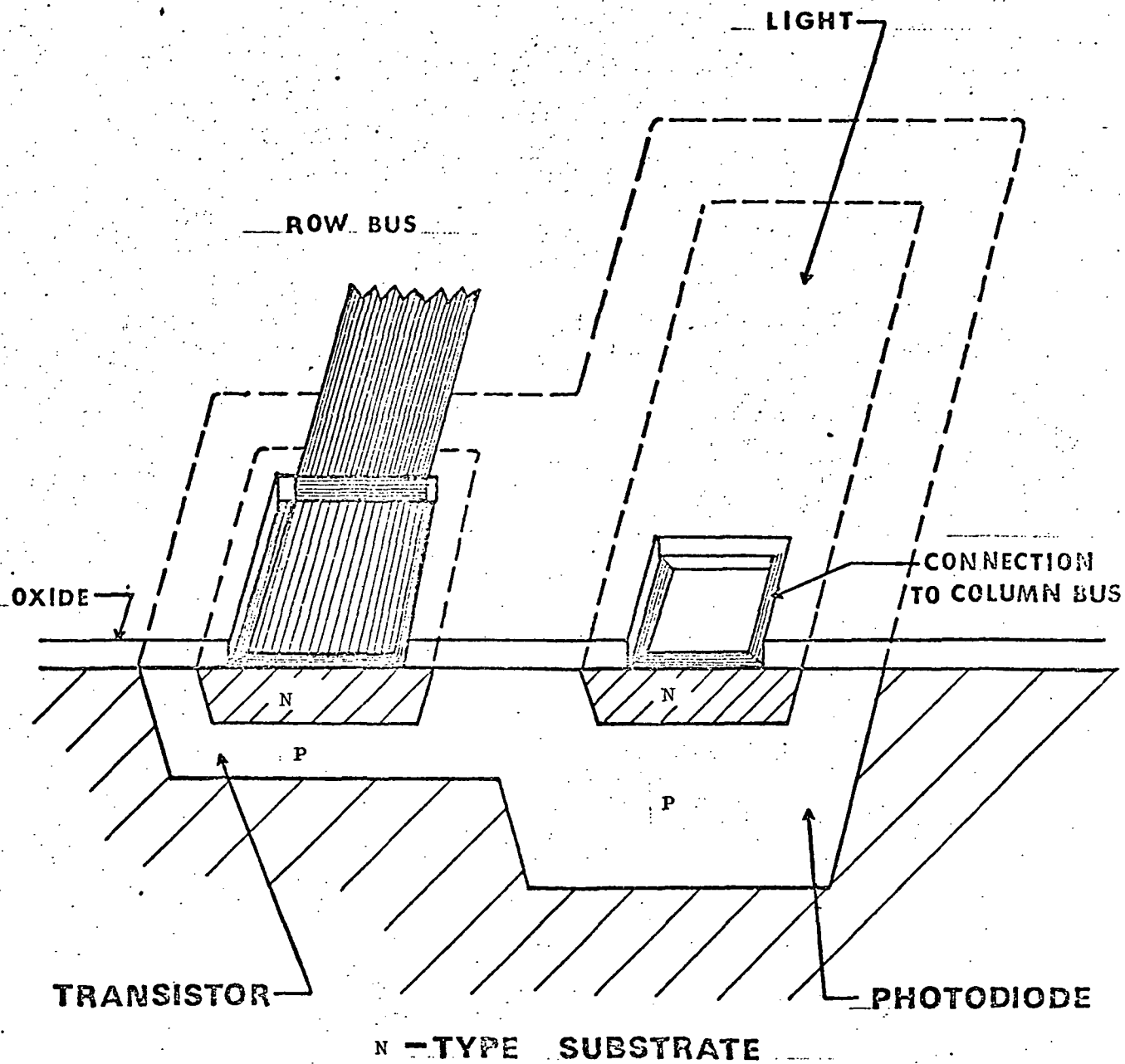


Fig. 3 Example of an integrated circuit design for a photodiode transistor element.

The following is a step by step procedure for the fabrication of the photodiode-transistor image sensor. The masks used are standard sizes with .020" centers and are all negative (clear images). The cleaning procedures used and referred to below are described in detail at the end of the fabrication procedure. A detailed description of the photolithographic method using the AZ-1350J photoresist is also presented. The wafers used are received polished and cleaned from the manufacturer.

Wafers: n-type, 1 Ω -cm, phosphorous doped, <111> orientation, ~0.10" thick, ~1.25" in diameter.

Clean: Procedure A

Oxidize: 45-min., 1200°C furnace temperature, wet N₂ method, 80°C water temperature, 150 cc/min N₂ bubbling through water subsequently mixed with another 200 cc/min N₂ prior to entering furnace. Line is heated to prevent condensation of water vapor carried by the gas before entering furnace. Estimated oxide thickness 0.395 μ .

Apply AZ: Open four .320" x .320" windows.
Photoresist:

Etch: 3.5-min. in 5:1 buffered HF.

Clean: Procedure B

Oxidize: 45-min., 1200°C furnace temperature, wet N₂ method, 80°C water temp., 150 cc/min N₂ bubbling through water bath mixed with another 200 cc/min N₂.

Apply AZ: Open deep well windows. They are 15 x 15 mils² windows except in one corner a 5 x 5 mils² area is not opened (See figure). Apply photoresist also in the back of the wafer so that the oxide will not allow Boron to diffuse in that side.

Etch: 4-min in 5:1 Buf. HF.

Clean: Procedure B

Activate: the BN type M slices used for B deposition for one hour, 950°C furnace temperature, 1000 cc/min O₂ flow. This step is performed in the Boron deposition furnace and at the same time as wafers are prepared for deposition.

Deposit B: 10-min, 850°C furnace temp., 380 cc/min N₂.

ρ_s : 160-170 Ω/\square . This is the surface resistance measured at different points on a test wafer. The test wafer is treated identically to and simultaneously with the sample wafer.

Transfer: wafers to drive-in furnace (same as oxidation furnace) without removing from hood or in any way treating wafers. Blow off any dust on test wafer with forced dry N₂ gas.

Drive-in: 40-hours, 1150°C (1200°C in the future) furnace temp., 200 cc/min O₂ plus 800 cc/min N₂ for the first 17 hours and no O₂ for remaining 23 hours.

Estimated: oxide thickness over deep well 0.575μ
(Inferred from etching time and oxide color of test wafer).

ρ_s : 140-160 Ω/\square on test wafer. The value of ρ_s for the deep well is assumed to be the same.

Apply AZ: Open 5 x 5 mils² base region at the corner left covered during opening of deep well. Again cover back side with photoresist.

Etch: 8-min., 5:1 Buf. HF.

Clean: Procedure B

Activate: BN slices as described above.

Deposit B: 10-min., 850°C furnace temp., 380 cc/min N₂.
New test wafer inserted.

ρ_s : 160-170 Ω/\square

Transfer: wafer to drive-in furnace without any treatment.

Drive-in: 1-hour, 1200°C furnace temp., wet N₂ oxidation used, 80°C water temp., 150 cc/min N₂ bubbled through water mixed with another 200 cc/min N₂ before entering furnace.

Estimated: oxide thickness over base 0.425μ . Oxide color gold.

ρ_2 : 600-680 Ω/\square on test wafer.

Apply AZ: Open photodiode windows over most of the area of deep well. In the figure it is the area enclosed by the dotted line.

Etch: 8 min., 5:1 Buf. HF.

Clean: Procedure B

Deposit

Phosphorous: 10-min, 850°C furnace temp., 6 cc/min Ar, bubbled through room temperature POCl_3 , mixed with 15 cc/min O_2 plus 800 cc/min Ar before entering furnace. Allow 1 min. after inserting wafer in furnace before turning on Ar bubbling through POCl_3 , while other gases are on.

ρ_s : 128 Ω/\square on test wafer with deep B diffusion.

Transfer: wafer to drive-in furnace without any treatment.

Drive-in: 2-hours, 1100°C furnace temp. wet N_2 oxidation, 80°C water temp., 150 cc/min N_2 bubbling through water mixed with 200 cc/min N_2 before entering furnace.

ρ_s : 60-80 Ω/\square on test wafer with deep B diffusion.

Estimated: oxide thickness 0.52 μ

Apply AZ: Open 2 x 4 mils² emitter windows.

Etch: 8-min, 5:1 Buf. HF.

Clean: Procedure B

Deposit P: 30-min., 1000°C, gases as previously described. Turn Ar bubbling through POCl_3 0.5 min after insertion of wafer in furnace.

ρ_s : 7 Ω/\square on second test slice.

Soak: wafer in clean 5:1 Buffered HF for 10 sec to remove phosphosilicate glass. Rinse well with distilled water and dry.

Drive-in: 45-min, 1000°C furnace temp., wet N₂ oxidation, 80°C water, 150 cc/min N₂ bubbled and mixed with 200 cc/min N₂.

ρ_s : 5 Ω/\square on second test slice.

Junction Depths: Measured by beveling wafer and staining.

Deep well $x_j \cong 11\mu$

Photodiode $x_j \cong 1.33\mu$

Transistor Base
Collector $x_j \cong 3.3\mu$

Cleaning Procedures:

- A. 1) Soak 5-min Aqua Regia ($1 \text{ HNO}_3 : 3 \text{ HCl}$)
- 2) " 5-min 5% HF
- 3) " 5-min in hot $2 \text{ H}_2\text{O} : 1 \text{ H}_2\text{O}_2 : 1 \text{ NH}_4\text{OH}$
- 4) " 5-min in hot $2 \text{ H}_2\text{O} : 1 \text{ H}_2\text{O}_2 : 1 \text{ HCl}$
- 5) " 1-min $1 \text{ H}_2\text{O} : 1 \text{ HF}$ (50%)
- 6) After each cleaning step overflow rinse in deionized tap water for 2-min.
- 7) Rinse well with distilled water.
- 8) Blow off water from back side of wafer with forced dry N_2 gas.
- 9) Place back side of wafer on spinner and spin at 5000 rpm for 60 sec. to dry wafer.
- 10) Quickly transfer to boat and insert in furnace.

B. This procedure follows application of AZ-1350J photo-resist.

- 1) Rinse wafer with acetone from wash bottle
- 2) Soak 5-min in hot acetone
- 3) Transfer to a clean beaker with hot acetone and soak 5-min.
- 4) Transfer to beaker overflowing with deionized water.
(Do not allow acetone to evaporate for it may leave residue on wafer).
- 5) Soak 5-min in fresh $1 \text{ H}_2\text{SO}_4 : 1 \text{ HNO}_3$.
- 6) Overflow rinse 2-min in deionized water.
- 7) Soak 10 sec. in clean 5% HF
- 8) Overflow rinse 2-min in deionized water
- 9) Rinse well with distilled water

- 10) Blow off water from back side of wafer with forced dry N₂ gas.
 - 11) Place back side of wafer on spinner and spin at 5000 rpm for 60 sec for final drying.
 - 12) Quickly transfer to boat and insert in furnace.
-

Application of AZ-1350J positive working photoresist

- 1) Dry: oxidized surface or have fresh oxide grown on wafer.
- 2) Spin: 5000 rpm, 30 sec.
- 3) Apply AZ: from bottle and cover wafer, but do not allow photoresist to overflow.
- 4) Spin: 5000 rpm, 30 sec., 30 msec acceleration.
Estimated photoresist thickness $\sim 1\mu$
- 5) Bake: 5-min, 150-180°F on hotplate.
- 6) Expose: 8-sec. using the Kulicke and Soffa Model 682 mask aligner equipped with 200 watt mercury vapor source.
- 7) Develop: 30-sec in 1 H₂O : 1AZ-1350J developer. 15-sec mild agitation and 15-sec. soak in clean developer.
- 8) Overflow
rinse: in deionized water 2-min.
- 9) Rinse: with distilled water
- 10) Dry: by blowing back side with N₂ gas, placing in spinner and spinning at 5000 rpm for 60-sec.
- 11) Note: multiple exposures are permissible. Steps 6 through 10 may be repeated several times until desired pattern is obtained.
- 12) Postbake: 5-min, 150-180°F on hotplate.
- 13) Rinse: wafer with distilled water before etching.

This step removes the possibility that air may be trapped inside the pattern causing incomplete etching.

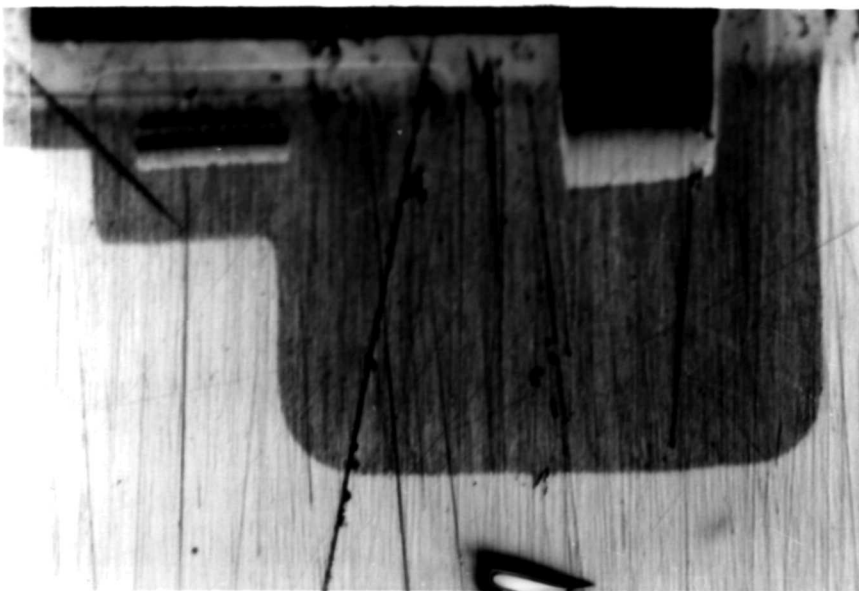


Fig. 4 Microphotograph of beveled and stained wafer, showing junction depths in the photodiode-transistor element.

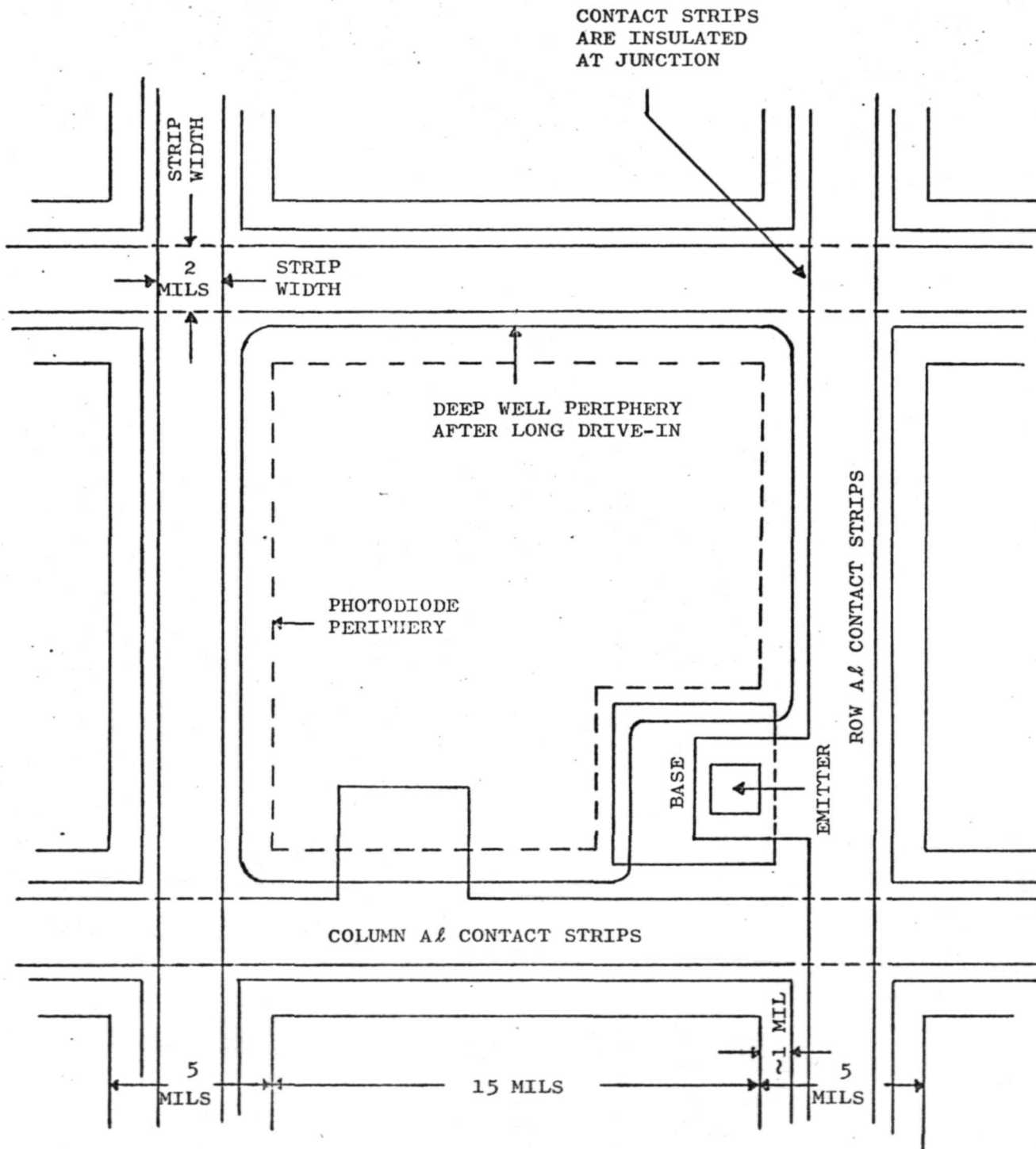


Fig. 5 Complete drawing of one element of the photodiode-transistor image sensor. This pattern is slightly different from those of the previous figures.

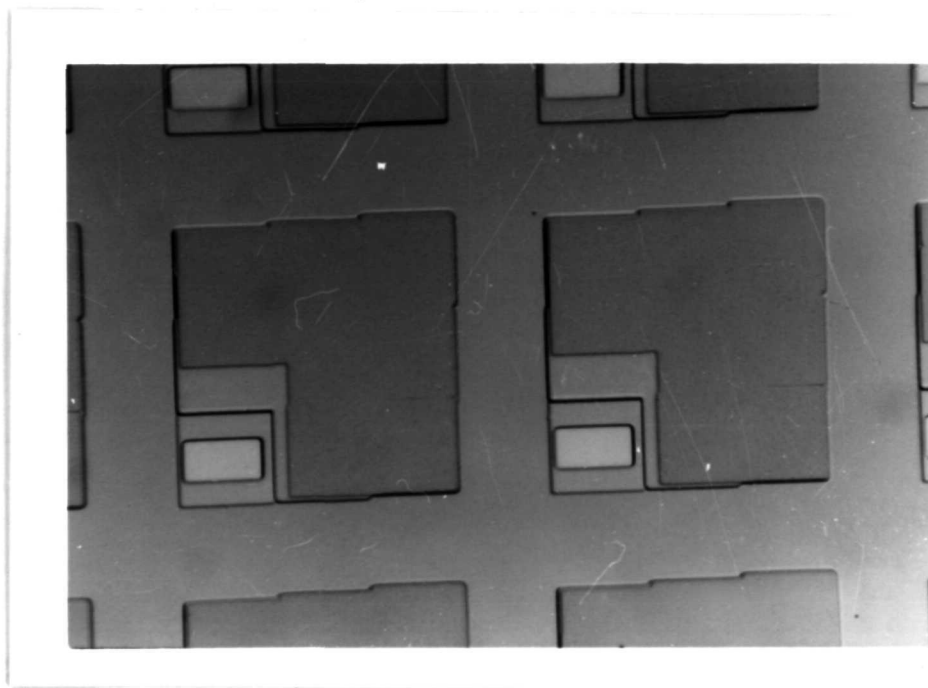


Fig. 6 Microphotograph of surface of processed silicon wafer. A Nomarski attachment was used in the microscope to enhance the contrast.

Figure 4 is a microphotograph of an element of the array. The wafer has been lapped at a 2° angle, and stained, to bring out the junctions. The deep and the shallow regions of the p-type well and the emitter and photodiode n-regions are clearly visible. The scratches and defects are due to the lapping process. This photograph corresponds to the sketch of Fig. 3.

The actual geometry being used for the more recent units is shown in Fig. 5. This differs slightly from the pattern of Figures 3 and 4 in that a larger area of the wafer is used for the photodiode, thus increasing the sensitivity of the array. A microphotograph showing the plan view of a portion of the array is given in Figure 6. The slight distortions in the picture are due to the Nomarski differential interference attachment which was used in the microscope to enhance the contrast between the various regions of the pattern.

c. Tests on Image Sensor Elements

As mentioned earlier, the metallization steps in the fabrication have not yet been successfully completed and hence scanning tests of the array have not yet been attempted. Tests on individual elements of the array were performed by using a wafer prober³ to make contact to the emitter and diode area of an element. It was desired to make tests which would give data on the performance of the element when in an array. For this purpose the circuit model shown in Figure 7 was used.

In Figure 7 four of the NXN elements of an integrated silicon array are shown. The voltages are such that element "A" is currently addressed. All other elements are in the storage mode. The transient and signal voltages appear across the emitter load

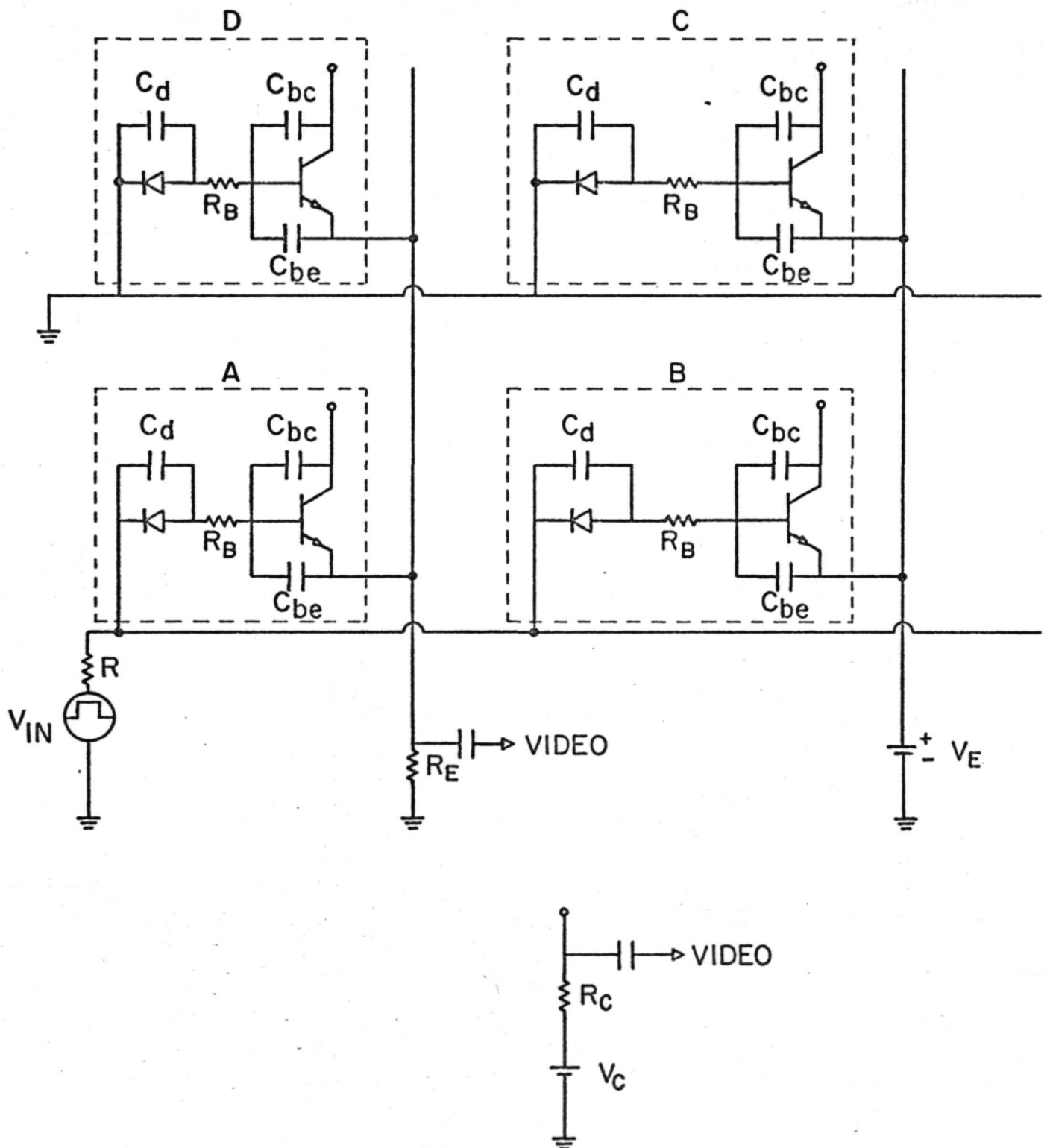


Fig. 7 Equivalent circuit model for tests on the array.

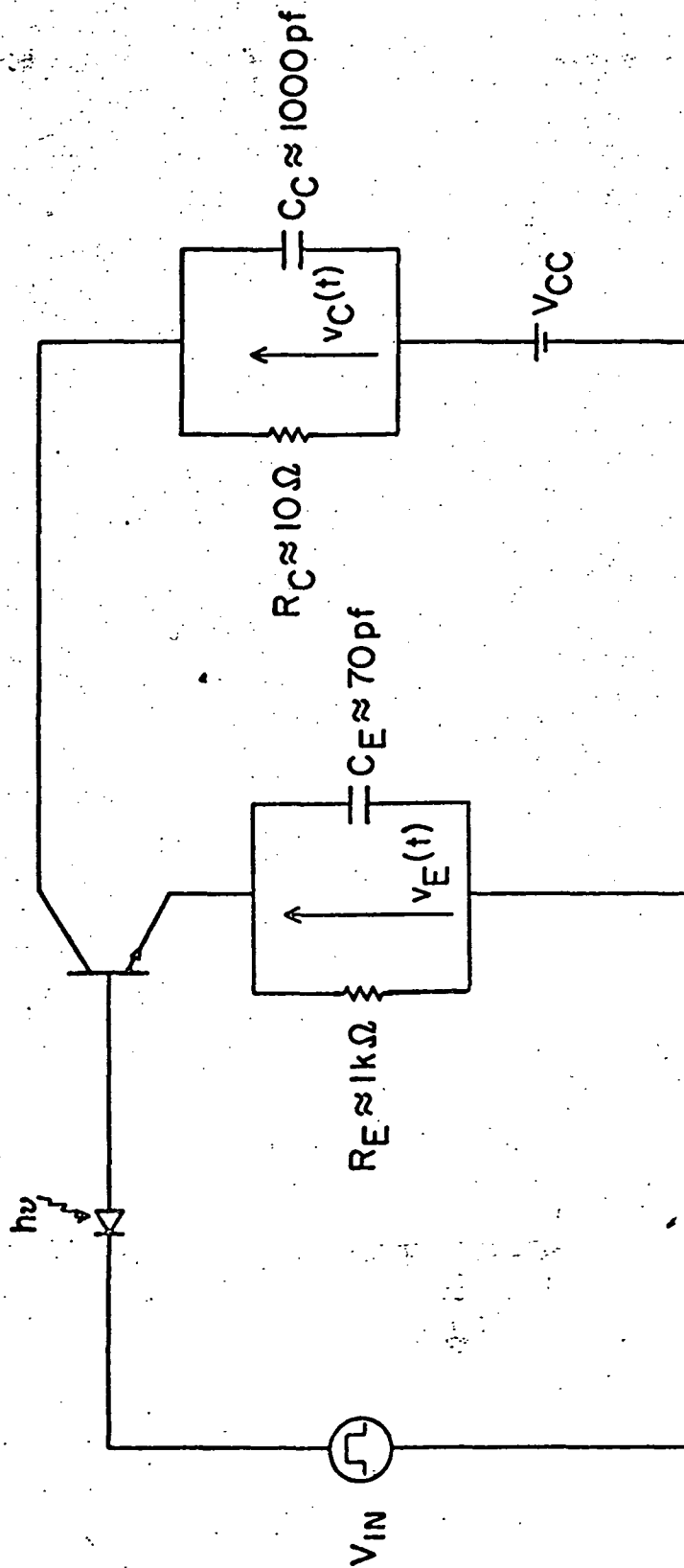


Fig. 9 Circuit used in tests on single elements of the array.

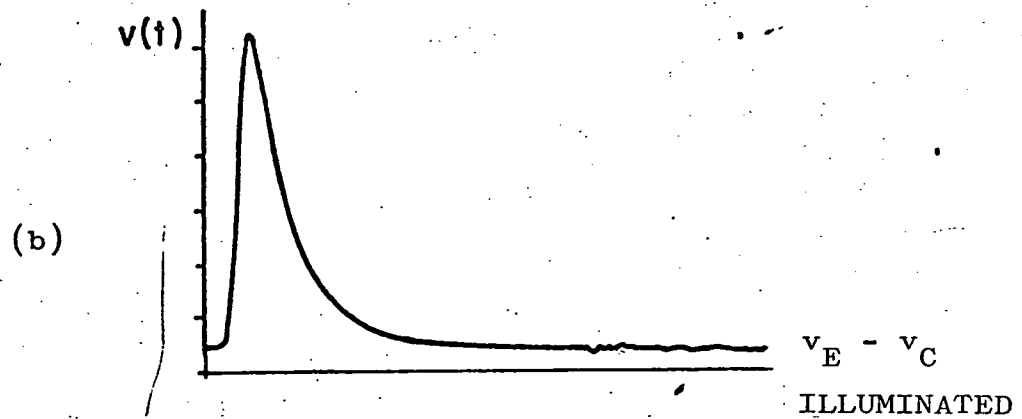
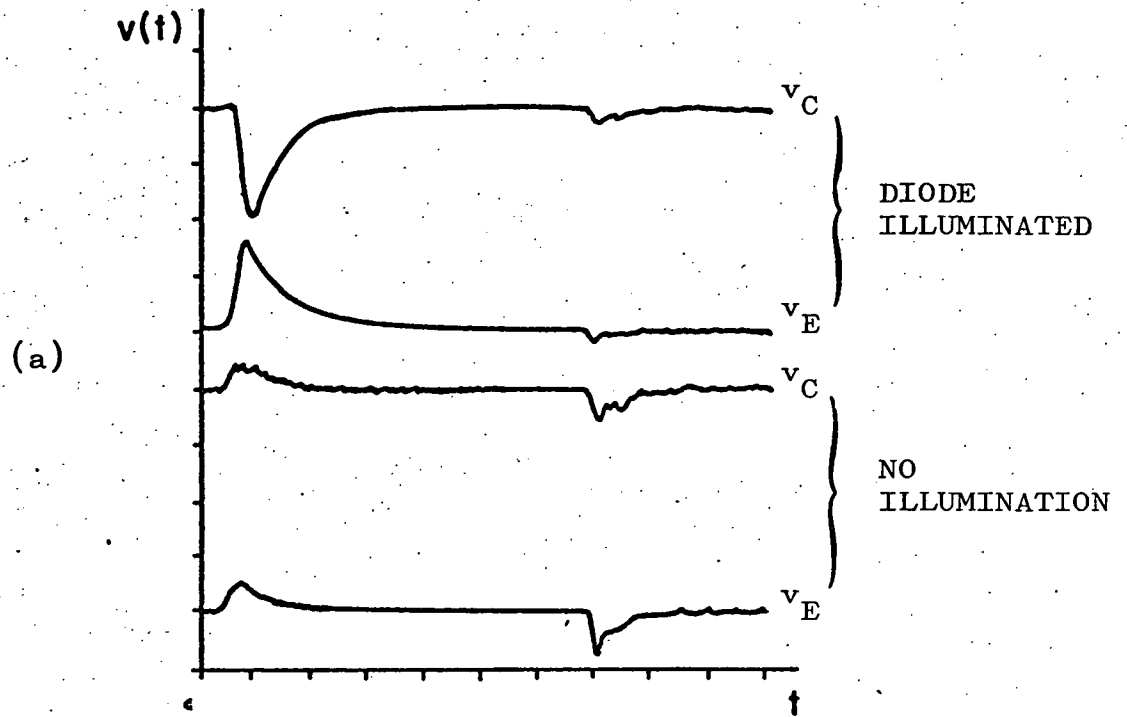


Fig. 10 Output signals from test element. The horizontal scale is $0.2 \mu\text{sec/division}$, the vertical scale is different for different traces.

resistance R_E and collector load resistance R_C . R_S is the source output resistance and R_B denotes the transistor base resistance. C_d is the photodiode junction capacitance and C_{bc} and C_{be} the base to collector and base to emitter junction capacitances. Because of the difference in area $C_d \gg C_{bc}$ and $C_d \gg C_{be}$, the equivalent circuit seen by the source is then as shown in Figure 8.

With the experimental values of some of the parameters in the figure and a few simplifying approximations, an analysis of the loading effect of the other elements on the element being tested can be calculated.

The tests were therefore conducted with these effects being simulated by external components. The diagram of the final circuit used for the pulse tests is shown in Figure 9. The choice of the values of R_E , C_E , R_C and C_C would simulate well the performance of an element in a 10 x 10 array.

Figure 10 shows tracings from an oscilloscope face during the test of a typical element. The driving pulse was a square one which had an amplitude of 1.1 volts and a duration of 1.2 μsec . The bottom two tracings of Figure 10 (a) show the emitter and collector transient voltages without any light falling on the photodiode. The transients are in phase as expected. The upper two traces were taken with the photodiode illuminated.

One of the principal features of the present array is that the signal to noise ratio can be greatly improved since both the above voltages are available. By inverting and amplifying one of the outputs and adding it to the other, the transients cancel while the signals add. The trace of Figure 10 (b) has been obtained in this way. The gain in signal to noise ratio is apparent in the figure.

III. SCANNING CIRCUITS

A system for scanning image sensor arrays and displaying the video signal was designed. The design is specifically for the photodiode-bipolar transistor array, but has enough flexibility that it can easily be adapted for other arrays which may have different scanning requirements.

Figure 11 shows the overall system. A fast shift register provides the column scanning pulses and a slow shift register the row scanning pulses. A set of clamping circuits and separate switches have been provided between the registers and the array. These will enable any polarity pulses with any D.C. level between -10V to +10V to be applied so that the system can be used for other types of arrays. Details of the synchronization which is controlled by a master oscillator are shown in Figure 12. Pressing the scan button loads the correct starting inputs to the shift registers. When the scanning starts, the shift registers act as ring counters. The sequential scan of the array continues until the reset button or the master switch is used to stop the register. The synchronization of the pulses can be understood from the timing diagrams of Figures 13 and 14. Figure 13 shows the timing diagram just after pressing the "Scan" switch; the timing diagram after initiation and completion of 17 cycles is shown in Figure 14. Signals taken from the horizontal and vertical counters go to D/A converters as shown in Figure 15 and the output from the converter positions the beam of an oscilloscope display (Tektronix type 604). Figure 16 shows a two-stage video amplifier (using a μ A 733) which enables the summation of the emitter and collector video signals with individually adjustable gains. The output of this amplifier

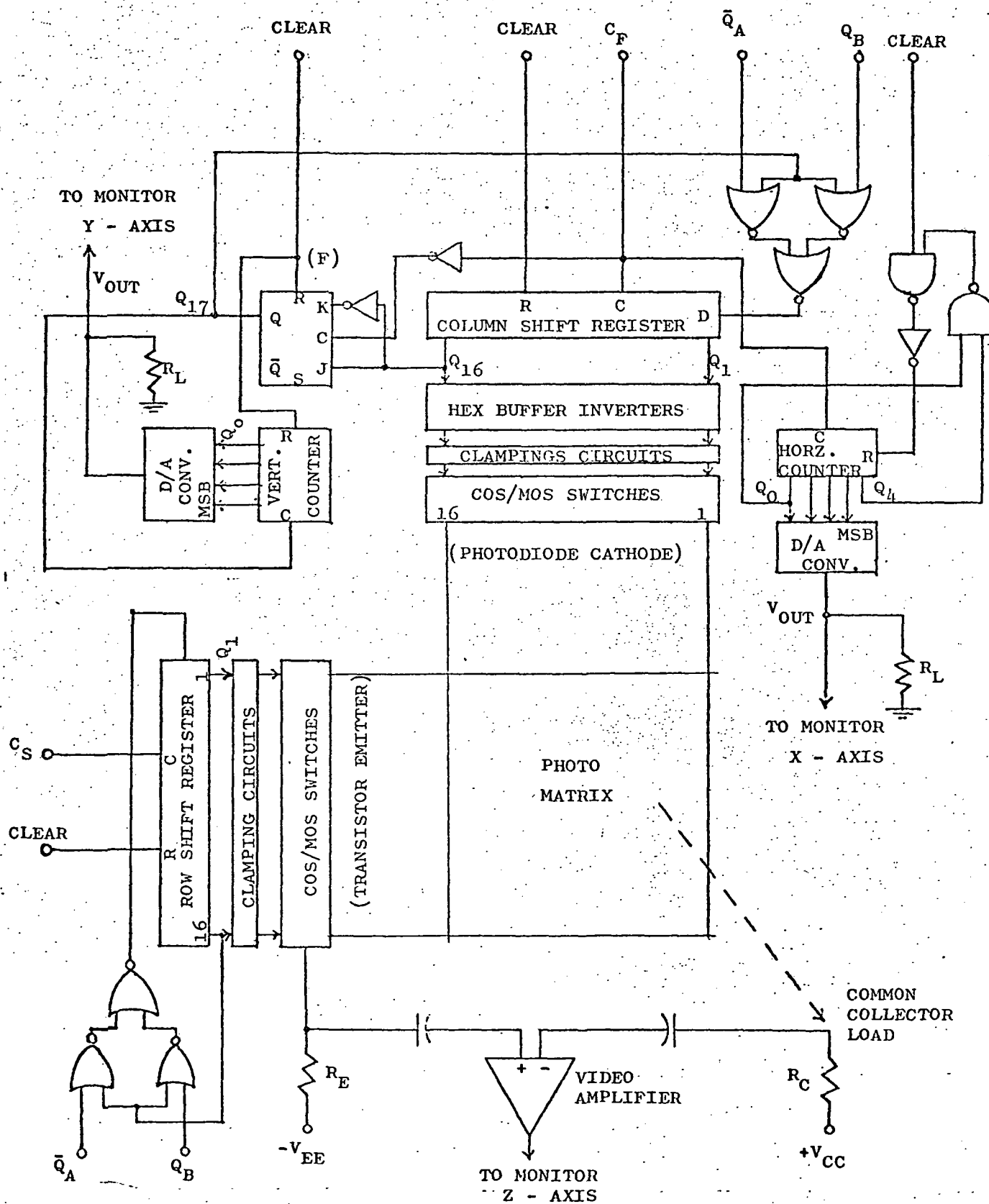


Fig. 11 Block diagram of scanning system for solid state image sensor arrays.

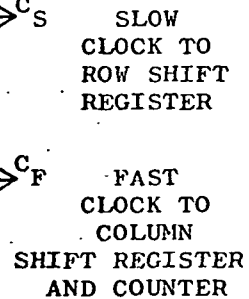


Fig. 12 Start and clocks synchronizer for scanning system.

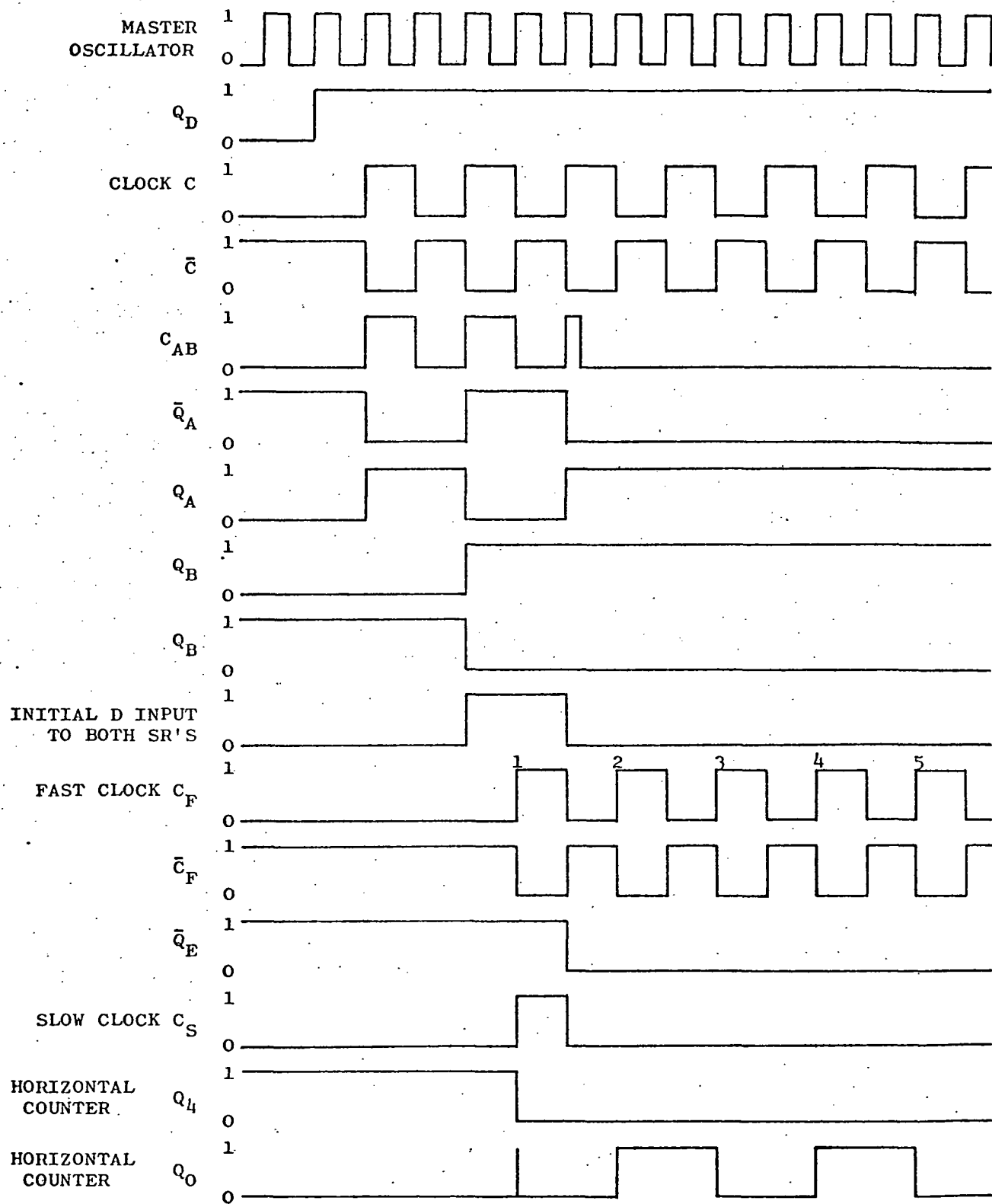


Fig. 13 Starting timing diagram just after pressing the "scan" switch.

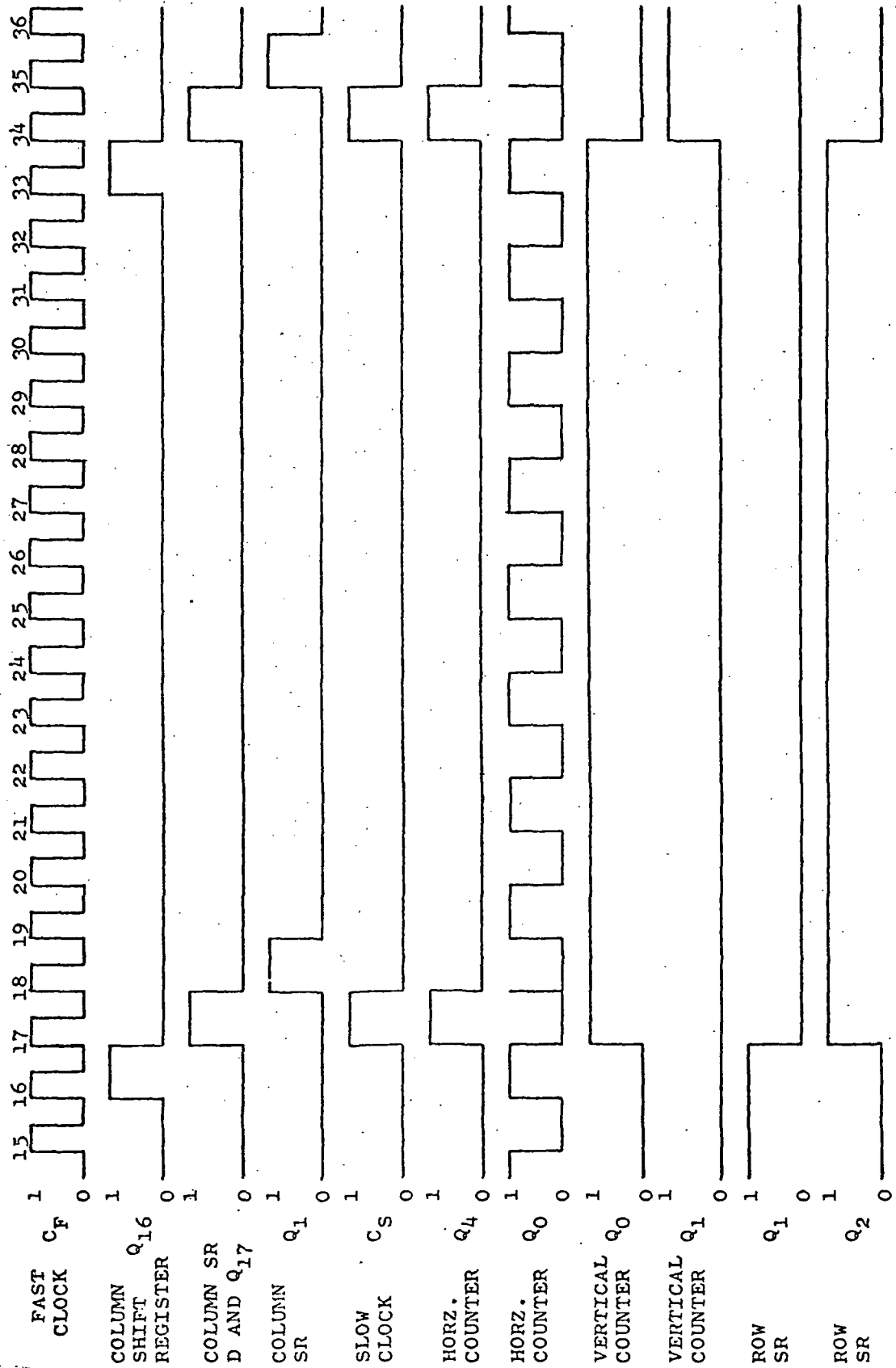


Fig. 14 Timing diagram seventeen cycles after initiation of scan.

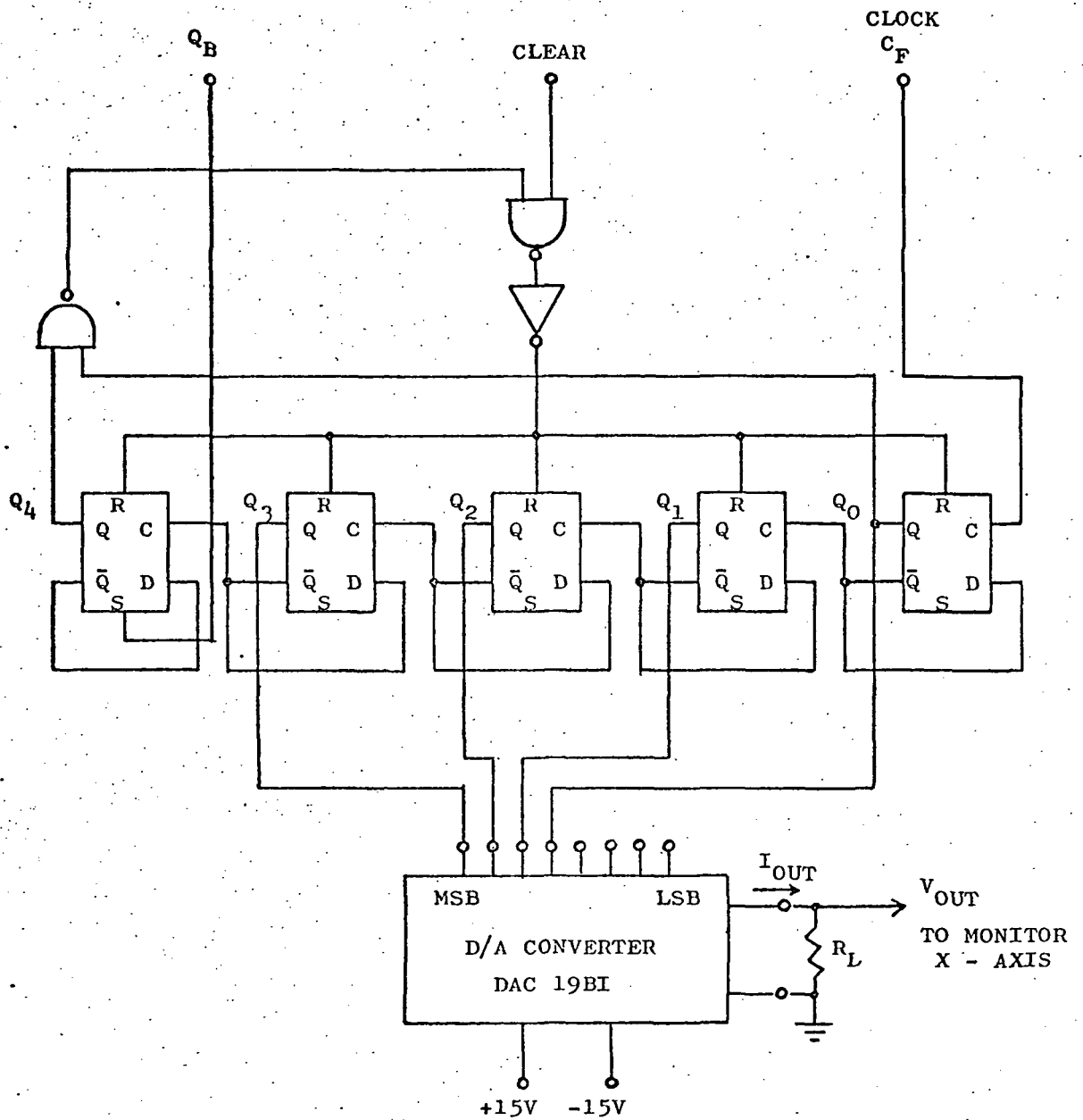


Fig. 15 Horizontal counter and D/A converter.

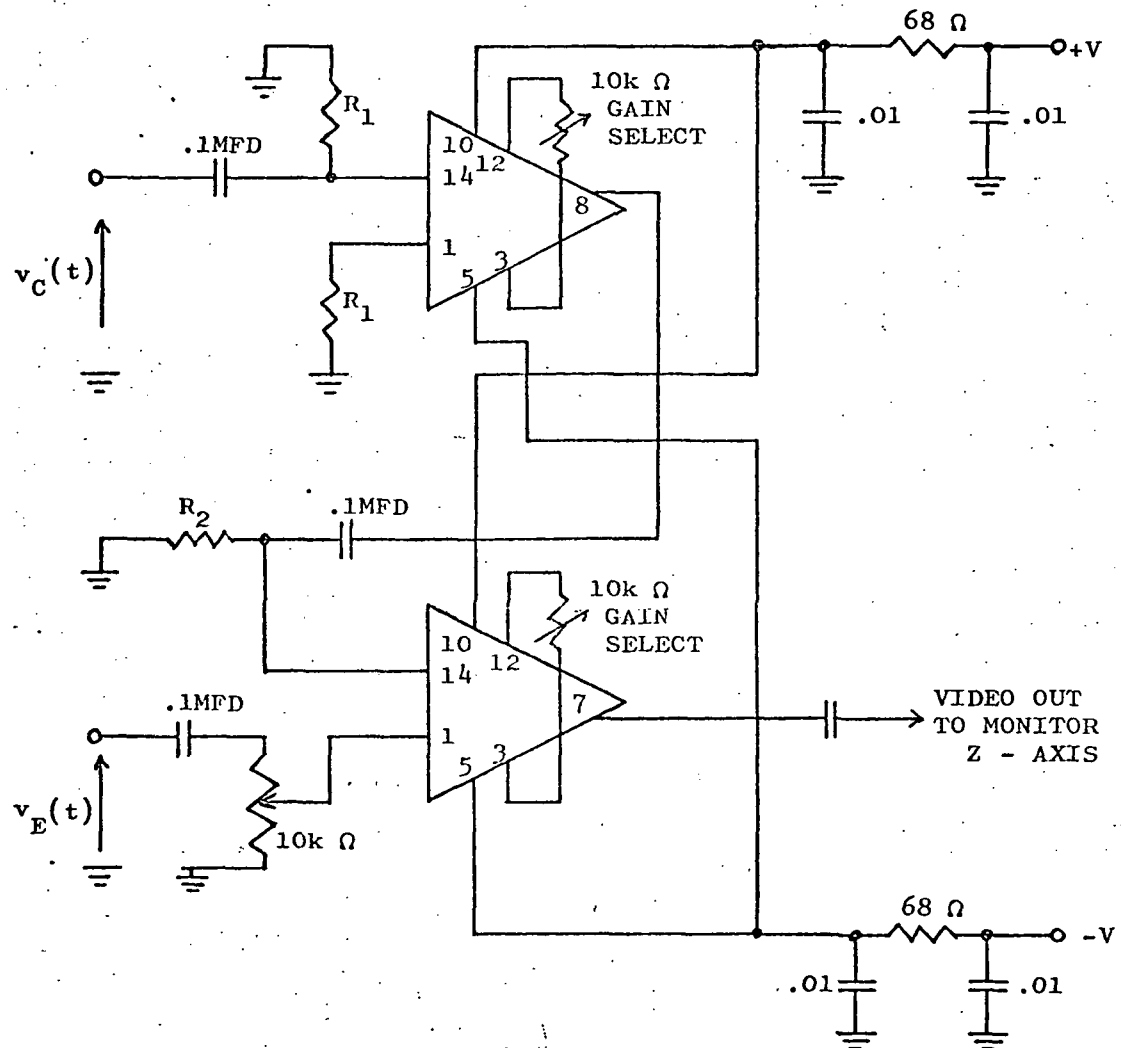


Fig. 16 Differential video amplifier circuit.

will go to the z-axis of the display oscilloscope.

Various parts of the scanning system have been breadboarded and tested. It is anticipated that the entire system could be put on two printed circuit boards.

The final design will have to be decided in conjunction with the metallization of the wafer in order to provide for the interconnections between the array and the scanning circuits.

IV. OPTICAL ABSORPTION EDGE IN SILICON

The use of extrinsic photoconductivity in silicon for detecting infrared radiation with sensor arrays implies the use of heavily doped silicon. Preliminary experiments were made on getting high Boron concentrations using the Boron nitride deposition and diffusion process. Junction depths of 20μ were achieved with reasonable uniformity.

The spectral response of p-n junctions was investigated as a possible simple way of characterizing heavily doped samples. Experiments with lightly doped samples were initially made in order to evaluate the method. It was found that this measurement provides a very valuable technique for studying optical absorption at very low levels. This is due to the fact that in this case the absorption is directly related to the measured photocurrent, whereas in reflection or transmission measurements the absorption is the small difference between two large measured quantities.

The experiments led to some new information on the optical-absorption edge of silicon. These were written up in a paper which has been accepted for publication by "Physical Review". A preprint of that paper is given in Appendix I.

V. HETEROJUNCTION STRUCTURES

Sandwich structures having evaporated Sb_2S_3 and gold layers deposited on a silicon wafer were fabricated. The samples were prepared in an NRC 3114 vacuum coater which has the following attachments:

- 1) A carousel with six boats which enables films of different materials to be successively deposited without breaking the vacuum.
- 2) A quartz crystal oscillator for monitoring the thickness and rate of deposition of the films.
- 3) A jig which enables mechanical masks to be moved under the substrate, so that the successive evaporations can be made in desired geometrical patterns on the substrate.

Masks were made which allowed the fabrication of $\text{Si-Sb}_2\text{S}_3\text{-Au}$ sandwiches with a semitransparent gold electrode. The external contact to the thin gold film was made by a thick gold film which was insulated from the silicon by an oxide layer. Thus the current-voltage characteristic across the structure could be measured with light incident through the substrate. The masks were designed such that four units were made on a single $3/4$ " diameter silicon wafer.

The current voltage characteristics of one sample in the dark and when illuminated with a tungsten lamp, with the light incident through the gold, are shown in Figure 17.

However, measurements on different samples with n- and p-type substrates of varying resistivities gave non-reproducible results as regards the direction of rectification and the light sensitivity.

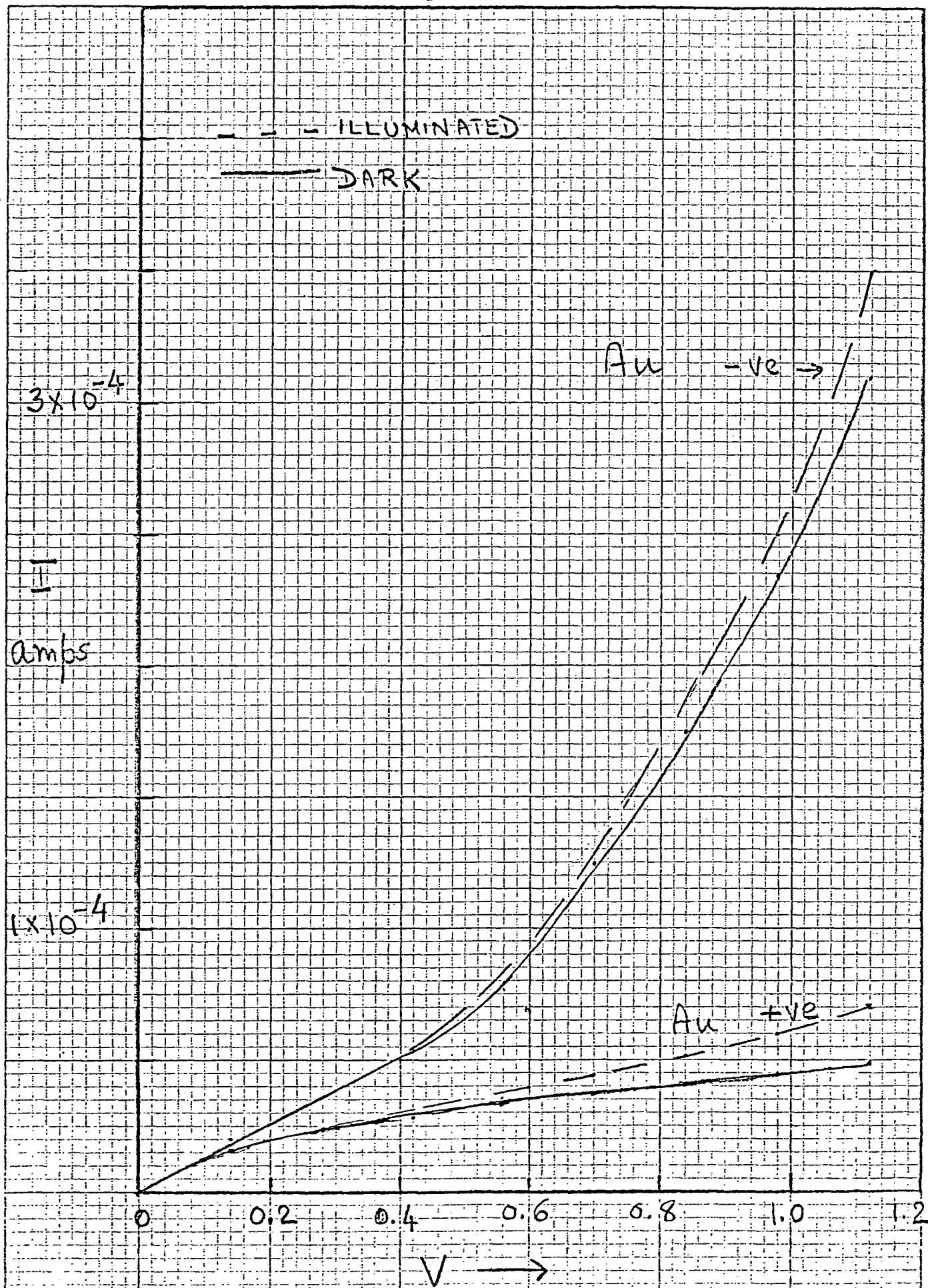


Fig. 17 Current-voltage characteristics of a Au-Sb₂S₃-silicon sandwich in the dark and when illuminated.

Various experiments were tried to locate the cause of this irreproducibility. At the moment it seems that contamination of the silicon surface is responsible for these effects. In the fabrication procedure the first step is the growing of an oxide on the silicon wafer, and etching away the oxide in the areas where the Sb_2S_3 is to be deposited. This step is needed for providing the stand-off insulation between the heavy gold connection to the top of the Sb_2S_3 and the silicon substrate. We believe that it is impurities introduced during the oxidation process which give rise to erratic surface conditions on the silicon wafer.

This hypothesis was suggested by measurements on MOS-capacitor structures which were fabricated in the system. The capacitance-bias characteristics of such structures were measured on a Boonton Capacitance Bridge, Type 75-C, and indicated the presence of a very large density of surface states.

The oxidation system was subsequently thoroughly cleaned, and modifications made. Recent samples of MOS capacitors made in the system have shown much better characteristics.

It was felt that it would be worthwhile to build a system for quick, routine measurement of capacitance-bias characteristics on wafers to aid in improving the processing steps. Figure 18 shows the system which has been assembled for this purpose, using a Boonton Capacitance Meter, Model 71CR. Figure 18 (a) shows the block diagram of the system and Figure 18 (b) the slow ramp generator for applying the bias.

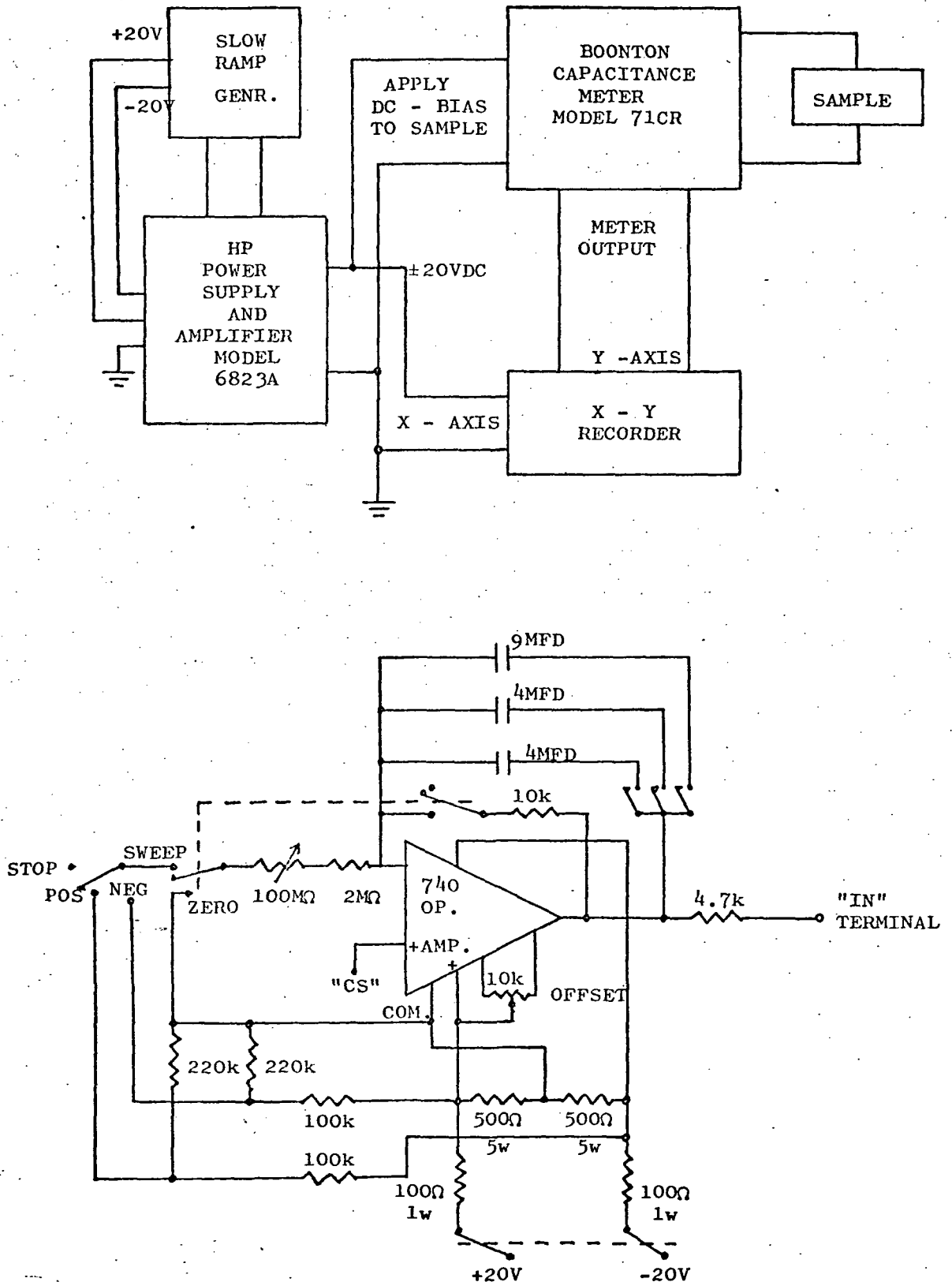


Fig. 18 Block diagram of CV measuring system for MOS capacitors. The lower diagram gives the details of the slow ramp generator.

VI. SUMMARY AND SUGGESTIONS FOR FURTHER WORK

The fabrication of a 16×16 element photodiode bipolar transistor array in silicon and tests on individual elements of the array have been described. A scanning system for the array was designed and breadboarded. The spectral response of p-n junctions was used as a technique for studying the optical absorption edge in silicon. A system for measuring C-V curves on MOS structures has been built, to be used for evaluating the Si-SiO₂ interface produced in our system.

The immediate steps suggested by the progress made are:

1. Complete the metallization steps in the fabrication of the array.

2. Build the scanning system, giving particular attention to interfacing with the wafer.

3. Perform scanning tests of the array and optimize the fabrication procedure for two kinds of applications.

- a) Sensitivity

- b) High speed addressing

4. Make measurements to enable characterizing heavily-doped silicon by the spectral response of photoconduction.

5. Continue the work on silicon-Sb₂S₃-metal sandwiches with the improved cleaning techniques for the silicon surface.

The long term objectives - devising arrays using heavily doped silicon, and heterojunctions for infrared sensing arrays, should be made according to the success achieved in items (4) and (5).

VII. STAFF PARTICIPATION

Principal Investigator - G. Sadasiv

Graduate Student - C. Anagnostopoulos

Considerable help was given in various phases of the project by Dr. G. Lengyel, Professor.

Some of the work on evaporated Sb_2S_3 films was done by Mr. James M. Aguiar, a student at the University of Rhode Island during the summer of 1972, under an NSF undergraduate research participation program.

REFERENCES

1. G. Sadasiv, "Device Analysis of Elements for Photosensor Arrays"
IEEE Solid State Sensors Symposium, Conference Record,
pp. 13-16, June, 1970.
2. The masks are purchased from Qualitron Corp., Danbury, Conn.
3. Electroglas Model 131.

FIGURE CAPTIONS

- Fig. 1. Equivalent circuit for a photodiode-bipolar transistor image sensing array.
- Fig. 2. Operation of a photodiode-bipolar transistor element.
- Fig. 3. Example of an integrated circuit design for a photodiode transistor element.
- Fig. 4. Microphotograph of beveled and stained wafer, showing junction depths in the photodiode-transistor element.
- Fig. 5. Complete drawing of one element of the photodiode-transistor image sensor. This pattern is slightly different from those of the previous figures.
- Fig. 6. Microphotograph of surface of processed silicon wafer. A Nomarski attachment was used in the microscope to enhance the contrast.
- Fig. 7. Equivalent circuit model for tests on the array.
- Fig. 8. Equivalent circuit seen by the source when addressing one element in the array.
- Fig. 9. Circuit used in tests on single elements of the array.
- Fig.10. Output signals from test element. The horizontal scale is $0.2 \mu\text{sec/division}$, the vertical scale is different for different traces.
- Fig.11. Block diagram of scanning system for solid state image sensor arrays.
- Fig.12. Start and clocks synchronizer for scanning system.
- Fig.13. Starting timing diagram just after pressing the "scan" switch.
- Fig.14. Timing diagram seventeen cycles after initiation of scan.

- Fig.15. Horizontal counter and D/A converter.
- Fig.16. Differential video amplifier circuit.
- Fig.17. Current-voltage characteristics of a $\text{Au-Sb}_2\text{S}_3$ -silicon sandwich in the dark and when illuminated.
- Fig.18. Block diagram of CV measuring system for MOS capacitors.
The lower diagram gives the details of the slow ramp generator.

APPENDIX I

FINE STRUCTURE IN THE OPTICAL ABSORPTION EDGE OF SILICON*

C. Anagnostopoulos and G. Sadasiv
Department of Electrical Engineering
University of Rhode Island
Kingston, Rhode Island 02881

Details of the structure in the indirect optical absorption edge of silicon were studied by measuring the dependence of the photocurrent in p-n junctions on the energy of the incident photons. The measurements were made at room and higher temperatures for photon energies $0.75 \text{ eV} < h\nu < 1.08 \text{ eV}$. The sensitivity of the method enabled high resolution measurements in the absorption tail. At room temperature, thresholds were found at $\sim 0.91 \text{ eV}$, 0.99 eV and 1.026 eV . The derivative of the response showed extensive fine structure in this tail. The TO and LO phonon assisted transitions to the ground and excited state of the exciton, previously reported in the phonon emission region, were seen here with phonon absorption occurring around 1.054 eV and 1.065 eV . There was additional structure in this region whose origin is not known.

I. INTRODUCTION

The optical absorption spectrum near the indirect band gap of silicon was measured by Macfarlane, McLean, Quarrington and Roberts¹ (MMQR). The absorption arises from indirect allowed transitions with momentum being conserved by the emission or absorption of a phonon. The electron-hole pairs created may either be unbound or exist as excitons with binding energy $\epsilon(n)$, where n denotes the n^{th} exciton level. The theory for the spectral dependence of the absorption coefficient α for such transitions was developed by Elliott². A summary of the theory and an analysis of the experimental results can be found in the extensive review by McLean³.

The agreement between theory and experiment was, in general, excellent, but there were a few discrepancies. The experimentally determined value of 5.5 meV for $\epsilon(1)$ - $\epsilon(2)$ led to an estimate of ~ 7 meV for the exciton Rydberg, whereas the value calculated from theory by McLean and Loudon⁴ was 14 meV. Another discrepancy involved the absence of any contribution from the longitudinal optical (LO) and longitudinal acoustic (LA) phonons, although transitions aided by these phonons are allowed. Finally, the experimental results showed absorption at photon energies lower than the minimum threshold energy for one-phonon aided transitions. The value of α in this absorption tail was

very small and could not be accurately determined from the transmission technique used by MMQR.

Dean et al⁵ measured absorption and luminescence at low temperatures and obtained results in substantial agreement with MMQR. The higher resolution they had enabled them to see additional structure near the thresholds which they attributed to splitting of the ground state of the exciton by valley-orbit interactions. Recently, Shaklee and Nahory⁶ presented results from wavelength derivative type experiments which indicated that the energy separation between the ground and first excited state of the exciton was 11.0 ± 0.2 meV, and the binding energy of the exciton was 14.7 ± 0.4 meV. In addition they pointed out theoretical reasons that preclude valley-orbit splitting of the exciton ground state. They identified the additional structure near the threshold for absorption of a photon with the emission of a transverse optical (TO) phonon as due to LO phonon assisted transitions. These results were later confirmed by Evangelisti et al in low temperature electroabsorption measurements⁷.

In this work we have investigated the dependence of the photocurrent generated in silicon p-n junctions on the energy of the incident photons. The ratio of the photocurrent to light intensity was measured and corrected to give the response R for constant photon flux. R was taken to be proportional to

the absorption coefficient α , which is true as long as the incident light is weakly absorbed. This point is discussed further in Section II. The sensitivity of the present method arises from the fact that α is directly related to the measured photocurrent, whereas in transmission or reflection experiments it is related to the small difference between two large measured quantities. The method proved particularly useful for measuring accurately the absorption tail. Measurements were also made in the TO phonon absorption region, i.e. where the absorption of a photon is accompanied by the absorption of a TO phonon.

The results can be summarized as follows:

- (1) At room temperature there are three prominent thresholds in the absorption tail. The first, which is not too well defined, occurs at 0.91 eV, the second at 0.99 eV and the third at 1.026 eV. The latter two were observed by MMQR. The first lies beyond their range of measurement.
- (2) The dependence of α on the photon energy following the latter two thresholds is not in agreement with that found by MMQR. This is due to the fact that there are a number of other lesser thresholds present.
- (3) In the region from 1.015 eV to 1.045 eV the results are accurate enough to permit numerical differentiation of the data to get the derivative of the response. The derivative plots show fine structure which has not previously been seen.

(4) The threshold energies and temperature dependence of α suggest that two and three phonon processes give rise to the absorption tail. The fine structure indicates that the phonons participating are not just from the Γ point and Δ symmetry direction of the Brillouin zone, but from throughout the zone.

(5) In the TO phonon absorption region our experiments show that there is more structure in the absorption coefficient than accounted for by the theory. Furthermore it is evident from our data that the fine structure, in the region following TO phonon aided transitions to the ground state of the exciton, has been the source of disagreement in previous determinations of $\epsilon(1) - \epsilon(2)$. The value of $\epsilon(1) - \epsilon(2)$ we find is in excellent agreement with that found by Shaklee and Nahory⁶.

(6) Finally, participation of LO phonons in the absorption process, first recognized by them in the region of phonon emission, is further confirmed in these experiments in the region of phonon absorption.

II. EXPERIMENTAL DETAILS

Commercially available large area silicon p-i-n photo-diodes and epitaxial n-on-p wafers were used. The n epitaxial layer was either phosphorous or arsenic doped and its thickness was approximately 15μ . The substrate was always boron doped and its thickness was of the order of 250μ . The resistivities of the epitaxial layer and the substrate were

the same in each sample and ranged in value between 1 and 10 Ω cm for different wafers. The measurements were made with the samples at room temperature and at higher temperatures.

A tungsten lamp, chopper and a double-grating monochromator with a spectral bandwidth of 0.5 nm were used to provide a chopped light beam. A beam splitter was used at the exit slit to irradiate the sample and a reference thermopile. The voltage developed across a load resistor connected across the sample was measured with one lock-in amplifier and the output from the thermopile on a second lock-in amplifier. The ratio of the outputs from the two lock-in amplifiers was measured with a ratiometer and recorded. This reading was multiplied by $1/\lambda$ to give R the response at different wavelengths for constant photon flux. The illumination level was kept low enough that the photocurrent varied linearly with light intensity. R is then proportional to the total number of electron-hole pairs created within an effective collection region near the junction.

The reasons for taking R to be proportional to α are as follows. In traversing a distance l the light is attenuated from intensity I_0 to $I(l)$ where $I(l) = I_0 \exp(-\alpha l)$. In the region of interest α is less than 1 cm^{-1} , and with wafer thickness of 250μ , we have $\alpha l \ll 1$. Hence $I_0 - I(l) \approx I_0 \alpha l$ and the light absorbed in the effective collection region is proportional to α . We assume the quantum efficiency to be

independent of photon energy. This assumption is substantiated by the photoconductive measurements made on germanium by Moss and Hawkins⁸. They found that in the absorption tail their calculated absorption coefficient from photoconductive measurements was identical to that obtained by Macfarlane et al⁹ from transmission measurements. In the present work the fact that the response is proportional to the number of photons absorbed in the effective collection region and is independent of diode parameters was experimentally verified by shining the light through either surface of the wafer. Despite the large asymmetry of the junction depth relative to the sample surfaces, the response obtained was identical. There were five room temperature measurements of the response in the region from 1.015 eV to 1.045 eV. These included the p-i-n diode and several different epitaxial wafers. All runs gave results which were the same to within a multiplying factor.

The monochromator which was used in the experiments had a linear wavelength scale. Where extreme accuracy was required the data points were taken by manual setting of this scale. The derivative spectrum was obtained by taking the difference between the responses at wavelengths separated by 1 nm. This gave $\Delta R / \Delta \lambda$ rather than $\Delta R / \Delta h\nu$, but for small ranges of λ one is proportional to the other. The value of 1 nm for $\Delta \lambda$ was chosen for highest resolution consistent with discrimination against noise.

A number of steps were taken to make sure of the genuineness of the structure seen in the derivative plots. The correctness and linearity of the monochromator scale were checked by measuring persistent lines and doublets in atomic spectra. The accuracy and reproducibility of the settings was found to be better than 0.02 nm. Effects due to the grating and beam splitter were eliminated by using a near-infrared transmitting filter and polarizer in front of the entrance slit of the monochromator. This was verified by repeating the experiments with a second thermopile or a Ge photodiode in place of the sample. In neither case was any structure observed. The use of several different samples has already been mentioned. Finally the samples were heated and measurements made at temperatures 10 to 50°C above room temperature. Large changes in the shape of the absorption curve are not expected for such small temperature changes and, since the energy gap decreases with temperature, all genuine structure should appear displaced to longer wavelengths. All structure discussed in Section III showed this expected behavior. Incidentally, there was no structure found that was caused by the system.

III. EXPERIMENTAL RESULTS AND DISCUSSION

A. The Absorption Tail

The method was useful for photon energies below 1.077 eV. At higher energies α and R are no longer linearly related because of the large value of α , and the large background results

in loss of sensitivity. The only information beyond 1.077 eV that was obtained was the energy at which onset of transitions to the ground state of the exciton occurred with the simultaneous emission of a TO phonon. This threshold gave an easily identifiable peak in the $\Delta R/\Delta \lambda$ versus λ curve, and occurred at 1.1692 eV. The peak due to the onset of transitions to the ground state of the exciton involving the simultaneous absorption of a TO phonon was easily established and occurred at 1.0538 eV. The average of these two energies gives the room temperature (296 K) exciton indirect gap, i.e. the energy gap minus the exciton binding energy, as 1.1115 ± 0.5 eV. Half of the spacing between the two peaks gives the TO phonon energy to be 57.7 ± 0.5 meV. These values are in excellent agreement with previous results.

A semi-logarithmic plot of the response against photon energy in the region of the absorption tail is shown in Fig. 1. There is a measurable response at 0.775 eV, and it increases by about an order of magnitude on going to 0.90 eV. Not much can be said about the shape of the curve in this region, as the signal was too small to be measured accurately. The signal was just above the noise level at the low energy end and was determined with about 6 percent accuracy at 0.90 eV.

Towards higher energies the response rises sharply, with clearly observable thresholds at 0.91 eV and 0.99 eV. Various simple expressions were tried for describing the response between these two thresholds. The formula

$$R = 4.9 + 1.09 x + 0.56 \exp x \quad (1)$$

with $x = \beta(h\nu - h\nu_0)$, $\beta = 67 \text{ eV}^{-1}$, and $h\nu_0 = 0.925 \text{ eV}$ gave a good fit to the data in the region between 0.925 eV and 0.983 eV. According to this formula the response is an exponential superimposed on a background consisting of a constant and a linear term. The data in this region at $T = 331 \text{ K}$ was fitted by

$$R = 10.8 + 2.30 x + 1.20 \exp x \quad (2)$$

where β was again 67 eV^{-1} , and $h\nu_0$ was 0.916 eV. The shift of 9 meV in $h\nu_0$ is in agreement with the change in the energy gap due to the rise in temperature. The latter was measured from the shift of the TO absorption peak and was 9 meV. It is of interest to note that the raising of the temperature increased the response by a factor of about 2.15, as is evident from Eqs. (1) and (2).

The response between the second threshold and the TO absorption region is shown in greater detail in Fig. 2. The top curve is data obtained at 331 K and goes with the upper scale; the bottom curve is the room temperature data and goes with the lower energy scale. The top scale is shifted towards lower energy by 9 meV relative to the bottom scale to offset the change in energy gap with temperature; the arrow points to the TO absorption threshold for both the room and high temperature data. In the region from 0.99 eV to 1.05 eV,

MMQR fitted their room temperature data with an expression of the form

$$\alpha = a(h\nu - 0.989)^2 U(h\nu - 0.989) + b(h\nu - 1.021)^2 U(h\nu - 1.021) \quad (3)$$

where $h\nu$ is measured in eV, a and b are constants and U is the unit step function. This implies that the absorption rises as the square of the energy from thresholds at 0.989 eV and 1.021 eV. In trying to fit such an expression to our measurements one of the problems was to find the correct extrapolation of the response at lower energies and subtract it from the actual data. The mechanism giving rise to the absorption below 0.98 eV is not known, and there is some concern about extrapolating an increasing exponential. For want of a better procedure it was assumed that the same mechanism continued to operate beyond 0.98 eV, and the extrapolated value R_{ext} was found from Eq. (1). Fig. 3 shows the square root of the difference between the actual and extrapolated values against photon energy. The bottom two curves are room temperature data for two different samples, the top curve is for a heated sample. The energy scale for the heated sample has again been shifted by 9 meV relative to the scale for the room temperature data. Between (a) and (b) one can draw approximate straight lines, with nearly common origin for the three curves. The threshold thus established is 0.982 eV at room temperature, as compared to the value of 0.989 eV found by

MMQR. There is a break in the curve at point (b). This occurs at 1.0213 eV, and coincides with the second threshold of Eq. (3).

To a very rough approximation, one can fit the tail in this region according to the dependence suggested by MMQR. The agreement, however, is not very good. There are really no straight line portions in Fig. 3. There is more structure in the response than indicated by Eq. (3). The arrows point to places where a break is apparent in every one of the curves. The deviations between the experimental values and the curve calculated to give the best fit are well beyond the experimental error.

The structure in the response can be seen more clearly in the derivative plots. As explained in Section II, it was more convenient for handling the data to choose λ as the independent variable instead of $h\nu$.

In Fig. 4, $\Delta R/\Delta \lambda$ is plotted against decreasing wavelength in the vicinity of the threshold at 0.99 eV. The top curve is the room temperature data, and the bottom curve is the data at higher temperature for the same sample. The scales are offset, as in the previous figures, to facilitate comparison. The similarity of these curves is evident. It is clear that not one but two peaks are present. The photon energies corresponding to these peaks are 0.989 eV and 0.994 eV for the room temperature data, and are shifted by 9 meV towards lower energies at higher temperature.

Fig. 5 shows $\Delta R/\Delta\lambda$ against decreasing wavelength in the region from 1.22μ to 1.18μ . The points plotted are the average of five runs with each run showing essentially the same features, while averaging eliminated some of the noise. There are several features with different and well defined shapes; the photon energies corresponding to these features are noted in the figure. It is worth noting that the step increase denoted by (a) occurs at 1.0256 eV, which corresponds to point (c) of Fig. 3. Beyond (h) the derivative is dominated by the TO phonon peak and its thermal broadening.

The mechanism giving rise to the absorption tail and the fine structure is not known¹⁰. We can rule out the effects of the electric fields in the space-charge region, as the diodes gave the same results with and without applied bias. Extensive studies of luminescence spectra of pure and doped silicon samples at low temperatures have been made by Dean et al¹¹. The structures seen were identified with levels of excitons bound to neutral impurities, and multiphonon processes¹². In the present experiments the impurities are ionized and the energy levels due to bound exciton-ionized impurity complexes in silicon is an open question¹³. One might expect these to lie near the localized level for a single carrier around the impurity. The observed energies of the structure in the present work do not correlate well with the known levels introduced by the impurities. In addition, the

fact that As and P doped wafers with resistivities ranging from 1 to 10 Ω cm, and the p-i-n photodiode, gave identical results suggests that impurity effects are negligible. Thus although the effect of the impurities cannot be completely disregarded our results are more in accordance with multi-phonon effects as discussed below.

The conduction band minima in silicon occur in the [100] direction of the Brillouin zone, with the magnitude of the wave vector being about 0.85 times the magnitude at the zone boundary. The optical and acoustic phonons with this wave vector are the ones involved in the one-phonon aided transitions; the T0 phonon has energy 57 meV and the TA phonon has energy 18 meV. It is possible to have two and higher order phonon aided processes, provided the sum of the wave vectors of the phonons is equal to the above value. As pointed out by McLean³, transitions are possible with the simultaneous absorption of the above TA or T0 phonon and an 0 phonon (i.e., a zero wave vector optical phonon). The energy of the 0 phonon is 63 meV. Two phonon aided transition thresholds would be expected at 0.991 eV (For T0 + 0) and at 1.031 eV (for TA + 0); these agree approximately with the data of Fig. 3. The observed threshold at 0.911 eV could be attributed to absorption of three phonons (0 + 0 + T0). The temperature dependence of the absorption in the region from 0.925 eV to 0.983 eV is in agreement with this assumption. The probability of the simul-

taneous absorption of three phonons is given by the product of the occupation numbers n_1 of each of the phonons, where

$$n_1 = [\exp (h\omega_1/kT) - 1]^{-1} \text{ and}$$

k is Boltzmann's constant. From this the ratio of the absorption at 331 K to that at 296 K is calculated to be about 2.17 as compared to the ratio of 2.15 between Eqs. (1) and (2). Two and three phonon structure has been previously reported^{11,12,14,15}. Peaks in modulation, tunnelling and luminescence experiments were identified with combinations of TO, TA, O and S phonon energies, where S is the phonon connecting different conduction band minima. The detailed nature of the structure in our results shows that choosing phonons from only some high symmetry points and directions is inadequate. Calculations of two phonon effects using a wider sampling of phonons has been done only for Raman scattering, where the sum of the momenta of the phonons is zero. The two phonon spectra have been observed both in Raman effect¹⁶ and electron energy loss measurements¹⁷. Calculations along these lines for the absorption edge might be useful in analyzing the present experimental results.

B. TO Phonon Absorption Region

It was pointed out in the introduction that there is some disagreement in the literature with regard to the fine structure in the region of TO phonon aided transitions and its

interpretation. The data obtained in the present measurements in this region are shown in Fig. 6 where $\Delta R/\Delta \lambda$ has been plotted against decreasing wavelength. The solid curve in the figure is drawn through those features that are seen with the same shape and relative amplitude in all the results, i.e. different runs on different samples. At higher temperatures these features were present, correctly shifted towards lower energies.

Following the interpretation reported by Shaklee and Nahory⁶, we identify the peaks at (a) and (b) as the thresholds for transitions to the ground state of the exciton with the absorption of a TO and an LO phonon respectively. The peaks (d) and (e) correspond to the TO and LO phonon aided transition to the first excited level of the exciton. The energy separation between the ground and first excited level of the exciton is found to be 11.9 ± 0.5 meV. The energy of the LO phonon is calculated to be 55.9 ± 0.5 meV. The values for the phonon energies and exciton levels obtained are in excellent agreement with the values found by Shaklee and Nahory in the phonon emission region.

But there is a discrepancy between theory and experiment. From the theory² it would be expected that the derivative of α would have a $-\frac{1}{2}$ power dependence on the energy from the threshold at (a) to about 12 meV away; and a $\frac{1}{2}$ power dependence on the energy from a threshold 14 meV away from (a). Clearly this is not what happens. Instead at (c), about 6.4 meV away from (a), there is a step increase in the derivative

and, neglecting the fine structure, there is an almost linear increase commencing about 10 meV away from (a). This behavior is in good qualitative agreement with the results of MMQR. They interpreted a step-like increase 5.5 meV away from the TO phonon peak as the onset of TO phonon aided transitions to the first excited state of the exciton, and the almost linear increase in the derivative commencing about 10 meV away from the TO peak as due to band transitions. Dean et al⁵ found a step increase about 7.5 meV from the TO peak with band transitions commencing about 4.5 meV after the step. They also interpreted the step increase as the onset of TO phonon aided transitions to the first excited state of the exciton. In Fig. 2 presented by Shaklee and Nahory⁶ the derivative in the region of TO phonon emission shows a definite increase, though not step-like, commencing about 7 meV away from the TO peak. It is clear from their figure and Fig. 6 of the present work that the increase is not due to background contributions. Finally, in electroabsorption⁷ spectra of Si a broad negative valley was observed following the TO peak corresponding to transitions to the ground state of the exciton.

Shaklee and Nahory's interpretation of the fine structure is probably the correct one, as it leads to good agreement between the experimental and theoretical values of the exciton levels, and gives the right energies for the peaks in Fig. 6. There are some features in Fig. 6 which do not correspond to

any peaks noted by Shaklee and Nahory. Some of these, like the structure near (f), could be due to multiphonon effects. These effects would be more prominent in the present measurements which were done at elevated temperatures and in the phonon absorption region. However, the increase in the derivative 7 meV away from the TO peak cannot be due to two phonon effects or impurity effects. If it were it would appear symmetrically placed with respect to the exciton indirect gap. But, as has been pointed out, it has been observed on the high energy side of the TO peak in all the experiments, at low and high temperatures, and both in the phonon emission and phonon absorption regions. It thus appears to be related to the TO peak, and consequently to the exciton, but at the moment there is no explanation for it. It is of interest to note that in transmission type experiments with GaP a crystal whose band structure is very similar to Si, anomalous fine structure was also observed for some of the phonon-assisted transitions¹⁸.

FOOTNOTES

*Work supported in part by NASA under Contract No. NGR40-004-022

1. G. G. Macfarlane, T. P. McLean, J. E. Quarrington and V. Roberts, Phys. Rev. 111, 1245 (1958).
2. R. J. Elliott, Phys. Rev. 108, 1384 (1957).

The spectral dependence of α is given by

$$\alpha \sim [h\nu - \epsilon_g + \epsilon(n) \pm h\omega_i]^{\frac{1}{2}} U(h\nu - \epsilon_g + \epsilon(n) \pm h\omega_i)$$

where $h\nu$ and $h\omega_i$ are the photon and phonon energies, ϵ_g is the energy gap, and U the unit step function. The upper sign corresponds to the absorption and the lower to the emission of the phonon. The sharp rise from a threshold will be smoothed out by thermal broadening of the exciton levels. The absorption coefficient due to the creation of unbound hole-electron pairs has the form

$$\alpha \sim [h\nu - \epsilon_g \pm h\omega_i]^{3/2} U(h\nu - \epsilon_g \pm h\omega_i).$$

The derivative of α will be proportional to the $-\frac{1}{2}$ and $+\frac{1}{2}$ power of the argument respectively in the two cases.

3. T. P. McLean, in Progress in Semiconductors, edited by A. F. Gibson, R. E. Burgess and F. A. Kroger (Wiley, New York, 1960), Vol. V., p. 53.
4. T. P. McLean and R. Loudon, J. Phys. Chem. Solids 13, 1 (1960).
5. P. J. Dean, Y. Yafet and J. R. Haynes, Phys. Rev. 184, 837 (1969).
6. K. L. Shaklee and R. E. Nahory, Phys. Rev. Letters, 24, 942 (1970).

7. F. Evangelisti, A. Frova and M. Zanini, Solid State Comm. 2, 1467 (1971).
8. T. S. Moss and T. D. H. Hawkins, Phys. Rev. Letters 1, 129 (1958).
9. G. G. Macfarlane, T. P. McLean, J. E. Quarrington and V. Roberts, Phys. Rev. 108, 1377 (1957).
10. For a recent review of absorption tail theories, see J. D. Dow and D. Redfield, Phys. Rev. B5, 594 (1972).
11. P. G. Dean, T. R. Haynes and W. F. Flood, Phys. Rev. 161, 711 (1967).
12. N. O. Folland, Phys. Rev., B1, 1648 (1970).
13. R. R. Sharma and S. Rodriguez, Phys. Rev. 153, 823 (1967).
14. Y. Yacoby, Phys. Rev. 142, 445 (1966).
15. A. G. Chynoweth, R. A. Logan and D. E. Thomas, Phys. Rev. 125, 877 (1962).
16. W. Kress, H. Borik, and R. K. Wehner, Phys. Stat. Sol. 29, 133 (1968).
17. B. Schroder and J. Geiger, Phys. Rev. Letters 28, 301 (1972).
18. P. J. Dean and D. G. Thomas, Phys. Rev. 150, 690 (1966).

We are grateful to the referee for pointing out the very relevant work of Evangelisti et al, ref. (7), Dean and Thomas (ref. 18), as well as references (11) and (12).

FIGURE CAPTIONS

Figure 1 - The photoresponse of silicon p-n junctions in the absorption tail. For reference the arrow points to the TO phonon absorption threshold.

Figure 2 - Expanded plot of response versus photon energy in the region from 0.96 to 1.06 eV. The upper curve has been shifted by 9 meV towards lower energies to offset the decrease in energy gap with temperature.

Figure 3 - Square root of the difference between the actual photoresponse and the extrapolated low energy response from Eq. (1), plotted against photon energy. The bottom curves are for different samples at room temperature. The top curve is for a sample at higher temperature, and has been shifted by 9 meV to facilitate comparison with the lower curves. The arrows point to structures seen in all the curves.

Figure 4 - $\Delta R/\Delta\lambda$ against decreasing wavelength near the threshold at 0.990 eV (1.250μ). The bottom curve has been shifted by 9 meV towards lower energies. The peaks for the top curve occur at ~ 0.989 eV and ~ 0.994 eV.

Figure 5 - $\Delta R/\Delta\lambda$ showing fine structure in the absorption tail.

The points are experimental values, the line is drawn through features seen consistently in all runs. The photon energies corresponding to the arrows are shown in the figure.

Figure 6 - The derivative of photocurrent with respect to wavelength for a silicon p-n junction, plotted against decreasing λ . The points are measured values of $\Delta R/\Delta\lambda$, the line is drawn through the features seen consistently in all runs. The peaks denoted by long arrows correspond to features seen by previous investigators. The photon energies in eV corresponding to the position of the arrows is shown in the figure.

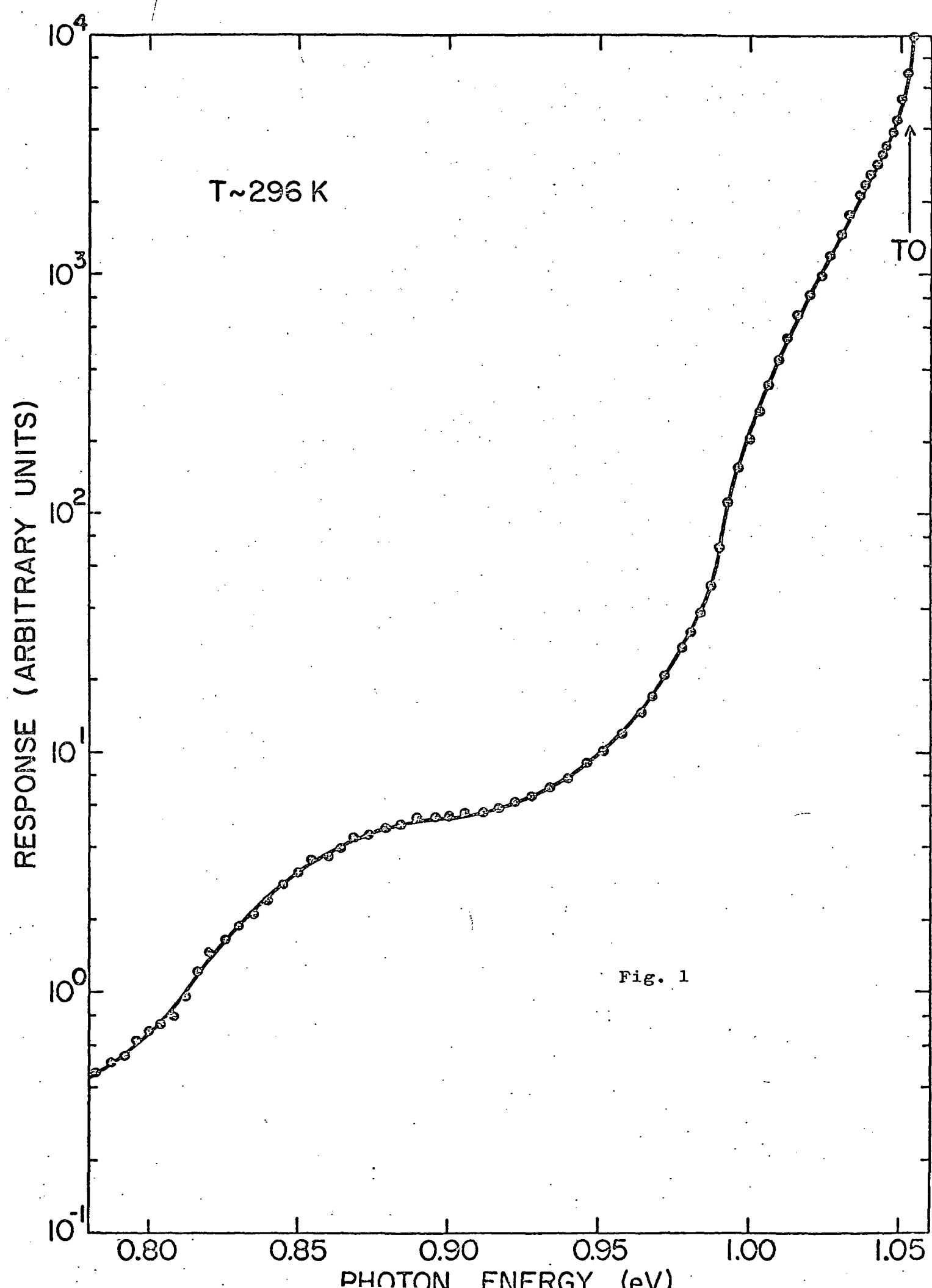


Fig. 1

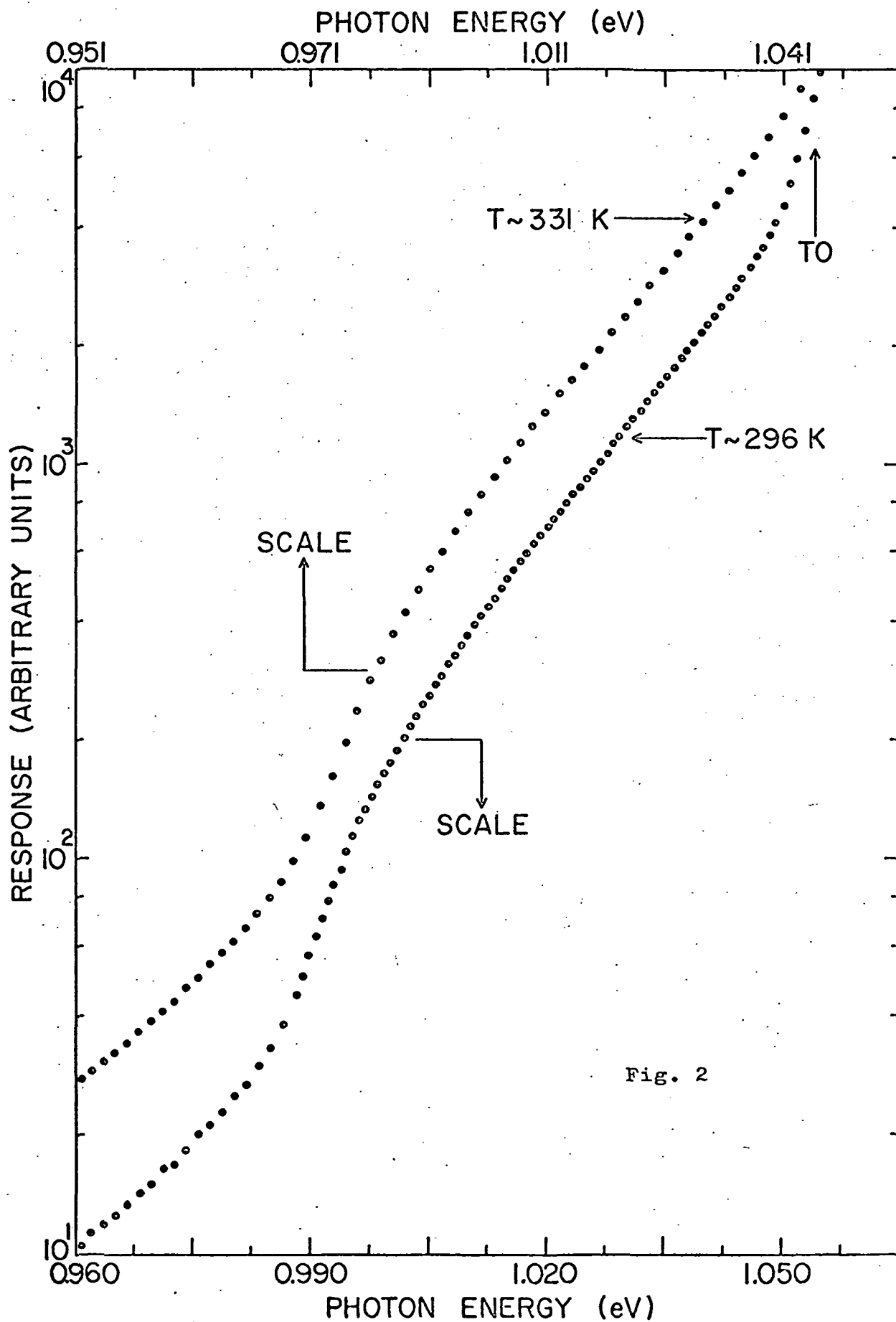


Fig. 2

